

REPORT DOCUMENTATION PAGE				Form Approved OMB No. 0704-0188	
<small>The public reporting burden for this collection of information is estimated to average 1 hour per response, including the time for reviewing instructions, searching existing data sources, gathering and maintaining the data needed, and completing and reviewing the collection of information. Send comments regarding this burden estimate or any other aspect of this collection of information, including suggestions for reducing the burden, to Department of Defense, Washington Headquarters Services, Directorate for Information Operations and Reports (0704-0188), 1215 Jefferson Davis Highway, Suite 1204, Arlington, VA 22202-4302. Respondents should be aware that notwithstanding any other provision of law, no person shall be subject to any penalty for failing to comply with a collection of information if it does not display a currently valid OMB control number.</small> PLEASE DO NOT RETURN YOUR FORM TO THE ABOVE ADDRESS.					
1. REPORT DATE (DD-MM-YYYY) 10-05-2010		2. REPORT TYPE		3. DATES COVERED (From - To)	
4. TITLE AND SUBTITLE Characterization and Comparison of New Concepts in Neutron Detection				5a. CONTRACT NUMBER	
				5b. GRANT NUMBER	
				5c. PROGRAM ELEMENT NUMBER	
6. AUTHOR(S) Sax, Kayla Jane				5d. PROJECT NUMBER	
				5e. TASK NUMBER	
				5f. WORK UNIT NUMBER	
7. PERFORMING ORGANIZATION NAME(S) AND ADDRESS(ES)				8. PERFORMING ORGANIZATION REPORT NUMBER	
9. SPONSORING/MONITORING AGENCY NAME(S) AND ADDRESS(ES) U.S. Naval Academy Annapolis, MD 21402				10. SPONSOR/MONITOR'S ACRONYM(S)	
				11. SPONSOR/MONITOR'S REPORT NUMBER(S) Trident Scholar Report no. 394 (2010)	
12. DISTRIBUTION/AVAILABILITY STATEMENT This document has been approved for public release; its distribution is UNLIMITED					
13. SUPPLEMENTARY NOTES					
14. ABSTRACT The purpose of this project was to to convert a low-power static random access memory (SRAM) chip into a neutron detector and then compare it to other standard neutron detectors. This project serves as a proof of principle for the use of memory chips as radiation detectors and provides insights about design parameters to chip designers, facilitating the development of the next generation of low-powered neutron detectors capable of providing real-time data.					
15. SUBJECT TERMS Neutron Detection, SRAM, dosimeter, Boron-10					
16. SECURITY CLASSIFICATION OF:			17. LIMITATION OF ABSTRACT	18. NUMBER OF PAGES 83	19a. NAME OF RESPONSIBLE PERSON
a. REPORT	b. ABSTRACT	c. THIS PAGE			19b. TELEPHONE NUMBER (Include area code)

Characterization and Comparison of New Concepts in Neutron Detection

MIDN Kayla J. Sax, USN

May 12, 2010

Abstract

The purpose of this project was to convert a low-power static random access memory (SRAM) chip into a neutron detector and then compare it to other standard neutron detectors. This project serves as a proof of principle for the use of memory chips as radiation detectors and provides insights about design parameters to chip designers, facilitating the development of the next generation of low-powered neutron detectors capable of providing real-time data.

Since commercially available memory chips are designed to minimize radiation influence, the chips were modified in order to increase their sensitivity to neutrons. This was accomplished by depositing a boron-10 (B^{10}) conversion layer near the active circuit components. When bombarded with neutrons, the conversion layer produces ionized products capable of changing the chips' memory state, thus indicating the presence of radiation.

This SRAM detection system was directly compared to a state-of-the-art powered helium-3 (He^3) system. Three non-powered detectors, bubble dosimeters, thermo-luminescent dosimeters, and track-etch dosimeters, were also evaluated. The detection systems were assessed using two polyethylene-moderated neutron sources, namely plutonium-beryllium and a deuterium-tritium neutron generator.

This study showed that, in comparison to conventional detection systems, the memory chips available for testing had in general a much greater dynamic range and provided reliable real-time data while operating at relatively low power. In addition, while they proved to be less efficient than the powered He^3 system, the memory chips modified with a B^{10} required much less power and revealed the potential for future sensitivity-enhancing modifications. This project has shown that the undoubtedly unique characteristics of a memory cell based detection system have the potential to improve existing technologies and enable important new applications such as those in health physics or homeland security.

Acknowledgements

Tackling this multidisciplinary project required the motivation and support of my four United States Naval Academy (USNA) advisers: Professor Martin E. Nelson (Mechanical Engineering), Professor Svetlana Avramov-Zamurovic (Systems Engineering), CAPT Charles B. Cameron (Electrical and Computer Engineering), and Professor James F. Ziegler (Physics). Without their guidance and willingness to dedicate countless hours to helping me grasp complicated concepts, this project would not have been possible.

Mr. Kelly Delikat, the USNA Technical Support Department's nucleonics laboratory technician, provided technical expertise and was a crucial member of my support team. He facilitated my experimentation, assisting me with neutron sources and data collection. On a daily basis, Mr. Delikat's common sense kept me grounded and sense of humor kept me sane.

In addition, several outside researchers contributed to this project. Dr. Kevin Jones, Chair of the University of Florida Materials Science and Engineering Department, hosted me during my summer internship and allowed me access to their facilities and laboratories. Dr. Mark Law, Chair of the University of Florida Electrical Engineering Department, provided insight about how to improve the memory-based detection system analyzed in this project. Dr. William Appleton, Director of the University of Florida Nanofabrication Facility, allowed me to work in the facility. Also from the University of Florida, PhD student Ray Holzworth and lab technician Al Ogden assisted me in the development of the sensitivity-enhancing chip modifications. Dr. Harold Hughes and Dr. Pat McMarr of Naval Research Laboratory's Solid State Device Branch were integral members of my adviser team throughout the project. They provided vital academic, technical, and financial support.

Contents

List of Figures	vi
List of Tables	viii
List of Symbols and Acronyms	ix
1 Neutron-Detection Systems	1
1.1 Overview of Neutron-Detection System Applications	1
1.2 Neutron Production and Classification	2
1.3 Neutron Interactions with Matter and Neutron Detection . . .	2
1.4 Conventional Neutron-Detection Systems	3
1.5 Non-Powered Neutron-Detection Systems Evaluated	5
1.5.1 TLD	5
1.5.2 Bubble Dosimeters	5
1.5.3 Track-Etch Dosimeters	7
1.6 Powered Neutron-Detection Systems: He ³ Proportional Counter	8
1.7 Current Detection Methods Based on Integrated Circuit Com- ponents	8
2 Utilizing Static Random Access Memories for Neutron De- tection	10
2.1 Related Work: Perforated Thin Film Coated Semiconductor Thermal Neutron Detectors	10
2.2 Static Random Access Memory Device Layout	11
2.3 Soft Error Phenomenon and Single Event Upsets	12
2.4 Commercial SRAMs as Neutron Detectors	14
2.5 Motivation for Sensitivity-Enhancing Modification	14
2.6 Modification Process	17

2.6.1	Etching Process	17
2.6.2	B ¹⁰ Deposition and Passivation	20
3	Experimental Set-Up at the United States Naval Academy	23
3.1	Functional Block Diagram	23
3.2	Neutron Source and Moderator	24
3.3	Detector Stand	29
3.4	Micro-Controller #1 and PC #1 (SRAM Core Operating Voltage Control)	30
3.5	Micro-Controller #2 and PC #2 (Method for Evaluation of SRAM Sensitivity)	33
4	He³ Interceptor™ Evaluation: Performance Metric and Results	36
4.1	Detector Output and Appropriateness of Comparisons	36
4.2	He ³ Interceptor™ Performance Metric	37
4.3	He ³ Interceptor™ Results	37
5	SRAM Evaluation: Performance Metrics and Results	39
5.1	SRAM Performance Metrics	39
5.2	Unmodified SRAM as a Control	40
5.3	Modified SRAM Design Considerations and Specifications	41
5.4	Modified SRAM Results	42
5.4.1	Thermal Flux Dependence	43
5.4.2	Core Operating Voltage Dependence	44
5.4.3	B ¹⁰ Conversion Layer Thickness Dependence	45
5.4.4	Thermal Neutron Detection Efficiency vs. Thermal Neutron Sensitivity	49
6	Detector Comparison, Conclusions and Future Design Recommendations	52
6.1	Comparison of He ³ Interceptor™ and Modified SRAMs	52
6.2	Modified SRAM Conclusions	53
6.3	Future Design Recommendations	54
A	Conventional Non-Powered Detection System Results	56
A.1	Conventional Non-Powered Detection System Limitations and Detection Mechanisms	56

A.2	Conventional Non-Powered Neutron Detection Systems Results and Suggested Performance Metrics for Future Works . .	56
A.3	Conventional Non-Powered Detection System Suggested Performance Metrics for Future Work	57
A.3.1	Bubble Dosimeter	58
A.3.2	Track-Etch Dosimeter	58
A.4	Recommendations for Future Work	59
B	Foil Activation Theory and Sample Calculations	60
B.1	Foil Activation Theory	60
B.1.1	Thermal Flux Determination	61
B.1.2	Fast Neutron Flux	63
B.2	Sample Calculations	64
B.2.1	Thermal Flux	64
B.2.2	Fast Flux	67

List of Figures

1.1	TLD card (left) and holder (right). The four sensitive areas are on the card and contain lithium fluoride (LiF) crystals. . .	6
1.2	Bubble dosimeter.	6
1.3	Track etch dosimeter.	7
1.4	Thermo Scientific Interceptor TM	9
2.1	Six-transistor SRAM schematic.	11
2.2	Pictorial representation of a single event upset.	13
2.3	Soft error rate trends from 1984–2004 (fails/bit).	15
2.4	Soft error rate trends from 1984–2004 (fails/chip).	16
2.5	Chip mounted on a 4 inch carrier wafer.	18
2.6	Loading of carrier wafer in deep reactive-ion etching chamber.	19
2.7	Chip after deep reactive-ion etching process has been completed.	19
2.8	Unmodified SRAM cross-section and modified SRAM cross-section and isometric representations.	22
3.1	Functional block diagram illustrating the experimental set-up required to interrogate the chip.	24
3.2	One of five PuBe slugs.	26
3.3	Thermo-Electron 14.3 MeV D-T neutron generator located in Rickover Hall.	27
3.4	Schematic of Rickover 073, the United States Naval Academy’s neutron generator room and control room.	28
3.5	Detector stand model shown flat with windows for neutron-detection systems.	30
3.6	Detector stand model shown curved.	31
3.7	Detector stand fabricated by the United States Naval Academy Project Support Branch supporting neutron-detection systems.	32
3.8	Rabbit 3000 microprocessor.	33

3.9	Current amplifier for micro-controller #1.	34
3.10	Xilinx Spartan-3 microprocessor.	35
4.1	Histogram of He ³ Interceptor™ data collected when exposed to PuBe with 3 in of polyethylene moderator.	38
5.1	Thermal neutron sensitivities of a modified SRAM when ex- posed to PuBe and 14.3 MeV D-T neutron generator.	43
5.2	Linear regression analysis of core operating voltage dependence.	45
5.3	Logarithmic regression analysis of core operating voltage de- pendence.	46
5.4	Cross-section of modified SRAMS with layer thicknesses. . . .	47
5.5	η_{SRAM} of B ¹⁰ Chips #1, #2, and #3 vs. B ¹⁰ thickness at various operating voltages.	48
5.6	η_{SRAM} of modified SRAMs.	50
5.7	S of modified SRAMs.	51

List of Tables

1.1	Advantages and disadvantages of non-powered and powered conventional neutron-detection systems.	4
3.1	Subsystems and their functions and measurement techniques. .	25
3.2	Characterization of the PuBe neutron generator environment with varying polyethylene thicknesses.	29
3.3	Characterization of the 14.3 MeV neutron generator environment with varying polyethylene thicknesses.	29
5.1	Labels and specifications of chips evaluated in project.	42
5.2	Thermal neutron sensitivities of a modified SRAM when exposed to PuBe and 14.3 MeV D-T neutron generator.	44
5.3	R^2 values for linear and logarithmic regression analysis of core operating voltage dependence.	44
5.4	Secondary radiation (lithium and alpha particle) energies at layer boundaries and energy deposited in active circuitry of modified SRAMs	47
5.5	η_{SRAM} of modified SRAMs.	49
5.6	S of modified SRAMs.	50
6.1	Comparison of He ³ Interceptor TM operating in “Surveillance Mode” and B ¹⁰ Chip #3 operating at 0.65 V.	53
6.2	Summary of conclusions resulting from experimental characterizations.	54
6.3	Summary of conclusions resulting from experimental characterizations.	55
A.1	Thermal neutron sensitivities of B ¹⁰ Chips #1 and #2 at various core operating voltages.	57

List of Symbols and Acronyms

α	alpha particle
Ah	ampere-hour
b	barn
B ¹⁰	boron-10
Ba	barium
Cd	cadmium
COTS	commercial, off-the-shelf
Cs	cesium
Cu	copper
CVD	chemical vapor deposition
D	deuterium
DRIE	deep reactive-ion etching
EBPVD	electron beam physical vapor deposition
η	thermal neutron detection efficiency
eV	electron-volt
F	flourine
FIT	failures-in-time (failures per billion hours)
γ	gamma
He ³	helium-3
HpGe	hyper-pure germanium
In	indium
Li ⁷	lithium-7
LiF	lithium-flouride
n	neutron
NRL	Naval Research Laboratory
p	proton
PC	personal computer
ϕ	neutron flux

PuBe	plutonium beryllium
Q_{coll}	cumulative collected charge
Q_{crit}	critical charge required for upset
R^2	coefficient of determination
S	thermal neutron detection sensitivity
SEU	single-event upset
SER	soft error rate
Si	silicon
SiO ₂	silicon dioxide
Si ₃ N ₄	silicon nitride
SNM	special nuclear material
SOI	silicon on insulator
SRAM	static random access memory
SRIM	The Stopping and Range of Ions in Matter
T	tritium
TLD	thermoluminescent dosimeter
u	atomic mass unit
USNA	United States Naval Academy
Xe	xenon
XeF ₂	xenon difluoride

Chapter 1

Neutron-Detection Systems

This chapter will provide background material necessary to understanding neutron-detection system applications, neutron production and classification, neutron interactions with matter, and conventional neutron detection systems that were evaluated by this project. This information provides a foundation for understanding how a memory-based neutron detection system is inherently different from conventional systems.

1.1 Overview of Neutron-Detection System Applications

Neutron-detection systems have been developed for a wide range of vital applications. In the field of health physics, which is concerned with radiation physics and radiation biology, neutron detectors function as personal dosimeters measuring absorbed ionizing radiation in human tissue, and as area monitors (or rem-meters). Specifically, the United States Navy uses the DT-702 thermoluminescent dosimeter (TLD) to measure personal neutron (n), gamma (γ), and beta exposure and the AN/PDR-70 to monitor the neutron radiation level in spaces on nuclear powered vessels. In addition to assuring human beings are not exposed to dangerous levels of radiation, neutron-detection systems are used in commercial nuclear power plants for monitoring spent atomic fuel and in-core and out-of-core reactor instrumentation. Neutron detectors have also been utilized as a method of verifying compliance with international nuclear weapons treaties, such as the Nuclear Nonproliferation Treaty. Finally, neutron detectors are being used for im-

portant homeland security applications. Cargo containers are occasionally screened for the presence of special nuclear material (SNM) at U.S. ports of entry by customs inspectors, outside these ports by border patrol agents, and on board ships entering the U.S. territorial waters by the Coast Guard. SNM is nuclear material that contains isotopes of uranium and plutonium which have the potential to be used as the fuel in nuclear weapons. SNM emits neutrons, making neutron detection of this material feasible.

1.2 Neutron Production and Classification

A desire to detect neutrons for the purposes outlined in Section 1.1 leads to the necessity of understanding neutron production. The most prolific source of neutrons is the nuclear reactor, in which uranium, plutonium, or thorium nuclei undergo fission, emitting multiple neutrons. The energy distribution of these fission neutrons peaks at 0.7 MeV and has a mean value of 2 MeV [1]. Fissioning also produces fission fragments, of which approximately forty types are neutron emitters [1].

Because the type of reaction a neutron undergoes depends highly on the neutron's energy, it is convenient to classify neutrons based on their kinetic energy. For the purpose of this project, neutrons are divided into two categories: fast neutrons and slow neutrons. The two classifications will be divided at about 1 eV, which corresponds to “the energy of the abrupt drop in absorption cross-section in cadmium” [2]. The term *thermal neutrons* will apply to slow neutrons that have approximately the same kinetic energy as molecules in their environment [1]. Because the most probable energy for neutrons at a standard temperature of 293 K is 0.025 eV, this energy is often implicit when discussing thermal neutrons.

1.3 Neutron Interactions with Matter and Neutron Detection

Because neutrons carry no charge, detecting their presence poses a significant challenge and detection mechanisms are often based on measurement of secondary radiation. Secondary radiations resulting from neutron interactions are often heavy, positively-charged particles (i.e. have an atomic weight greater than or equal to 1 u), which tend to have a very short range in liq-

uid or solid media. All neutron-detection systems directly detect secondary charged particles, such as protons (p) and alpha particles (α), created by the conversion of incident neutrons [2].

When considering thermal neutrons, important nuclear interactions involve elastic scattering off nuclei as well as an array of neutron-induced nuclear reactions. Since the kinetic energy of slow neutrons is relatively small, very little energy can be transferred to the nucleus in elastic scattering. Elastic scattering, therefore, is generally not a feasible interaction on which to base a thermal neutron-detection system. However, elastic scattering collisions have a relatively high probability of occurrence, often bringing fast neutrons into thermal equilibrium with the medium before any other interaction takes place. The most significant slow neutron interactions are neutron-induced reactions that create secondary radiations of adequate energy for direct detection. Due to low incoming neutron energy, these reactions must have a positive nuclear disintegration energy (or Q-value) to be energetically possible [2]. Because the secondary radiations are charged particles, reactions such as (n, α), (n,p), and (n,fission) are the most attractive for neutron detection [2].

Scattering nuclear reactions are more dominant in the case of fast neutrons than slow neutrons because the probability of most neutron-induced reactions in detectors drops significantly with increased neutron energy. Scattering allows for moderation, or slowing of fast neutrons to lower energies. The most efficient moderator is hydrogen because the neutron can lose up to all its energy in a single collision with a hydrogen nucleus [2]. In order for the neutron-induced reactions discussed in relation to slow neutrons to be useful in the detection of fast neutrons, an effective moderator must be used.

1.4 Conventional Neutron-Detection Systems

An understanding of conventional neutron-detection systems is important to the project for two reasons. First, conventional detection systems serve as points of comparison for the memory chip detectors characterized by the project. Second, understanding their inherent advantages and disadvantages helps one realize how a detection system based on memory chips is fundamentally different. Conventional neutron-detection systems are conveniently divided into two subcategories, non-powered and powered. As a group, non-

Detector Class	Advantages	Disadvantages
Non-Powered	<ul style="list-style-type: none"> • Require no external energy source. • Relatively inexpensive. 	Passive (can only be read after exposure).
Powered	Active (can be read at will).	Require a significant amount of power.

Table 1.1: Advantages and disadvantages of non-powered and powered conventional neutron-detection systems.

powered detection systems share advantages and disadvantages compared to powered detectors. They are attractive because they require no external energy source and, therefore, can operate in almost any environment. In addition, they are relatively inexpensive compared to more complicated powered detectors. The biggest drawback on non-powered detection systems is that they generally provide the user no instantaneous information. The information they provide about radiation exposure is only obtained after the detector has been removed from the environment and read. Non-powered detection evaluated in this project include the TLD, bubble dosimeter, and track-etch dosimeter. It is worth noting that unlike TLDs and track-etch dosimeters, bubble dosimeters provide the user information about neutron exposure about ten minutes following exposure.

While non-powered detectors are unrivaled in their simplicity and cost, some applications require information on radiation exposure more quickly and more often. In these cases, powered detection systems are utilized. Although these detectors have the inherent drawback of requiring an outside power source, they have the distinct advantage of being active, that is, of being interrogated or read at will. The powered detection system that was considered in this project was a He^3 proportional counter. The advantages and disadvantages of each detector class are summarized in Table 1.1.

1.5 Non-Powered Neutron-Detection Systems Evaluated

1.5.1 TLD

The TLD is a small, non-powered radiation detector commonly used by personnel working in radioactive environments to measure exposure to radiation (see Figure 1.1 on the next page). TLDs contain a class of inorganic crystals that measure ionizing radiation exposure by quantifying the amount of visible light emitted from the crystal in the detector when the crystal is heated. The amount of light emitted is dependent upon the radiation exposure. The most commonly used material for TLDs by the United States Navy is lithium fluoride (LiF). As the radiation interacts with the crystal it causes electrons in the crystal's atoms to jump to higher energy states, where they stay trapped due to impurities (usually copper, phosphorus, or magnesium) in the crystal, until heated. Heating the crystal causes the electrons to drop back to their ground state, releasing a photon of energy equal to the energy difference between the trap state and the ground state. By recording the relative light intensity as a function of time, the radiation exposure can be calculated. TLDs are extraordinarily practical because a single detector can be reused many times. The TLDs used in this experiment were typical of those used in the United States Navy for dosimetry purposes. They were obtained from and read by the Naval Dosimetry Center (NDC) in Bethesda, MD.

1.5.2 Bubble Dosimeters

Bubble dosimeters are vials containing 8 cm³ of clear, elastic polymer (see Figure 1.2 on the following page). The emulsion is made sensitive to radiation through the suspension of $10^4 - 10^5$ droplets (about 20 μm in diameter) in the polymer [3]. Pressure and temperature conditions are varied so that the liquid droplets become superheated or overexpanded. The liquid remains in this state unless it is sufficiently disturbed, producing a more stable state of equilibrium by flashing into a vapor. This phase transition requires some sort of nucleation trigger that can be provided by the charged particles produced by interactions with incident neutrons. As these charged particles pass through the emulsion, they deposit energy, producing local regions of high energy density that cause local vaporization. If the area of local vapor-



Figure 1.1: TLD card (left) and holder (right). The four sensitive areas are on the card and contain lithium fluoride (LiF) crystals.

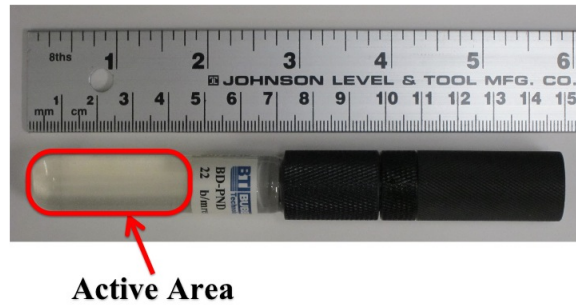


Figure 1.2: Bubble dosimeter.

ization surrounding the track reaches a certain critical size, it will result in further vaporization and the entire droplet will flash into a bubble of vapor. These bubbles are typically up to a millimeter in diameter [2]. As a result, the bubbles can be easily seen by simple visual inspection and indicate the presence of neutron radiation. Like TLDs, bubble dosimeters are reusable. The bubble dosimeters evaluated in this project were products of Bubble Technologies Industries (BTI), Chalk River, Canada [4].

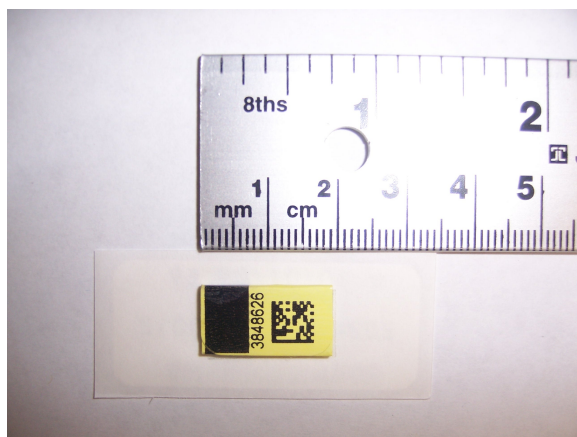


Figure 1.3: Track etch dosimeter.

1.5.3 Track-Etch Dosimeters

A track-etch dosimeter (see Figure 1.3) is a thin plate or film of a material that will register the track of an ionizing particle. Transferring energy to electrons, an ionizing charged particle passing through a dielectric material leaves a trail of damaged molecules along the particle track. This track becomes visible, in some materials, when etched in a strong acid or base solution. Materials utilizing this concept to detect particles are called track-etch dosimeters. When neutrons are the particles of interest, a converter such as lithium-6 (Li^6) or B^{10} is used in conjunction with a material that registers alpha tracks. Alternatively for neutron detection, a foil of fissionable material can be used to generate fission fragments that register in all track-etch materials. When the converter foil and registration material are kept in close contact, an image of the detected neutron distribution can be seen upon etching. Unlike TLDs and bubble dosimeters, track-etch dosimeters are not reusable. The track etch dosimeters and exposure reports were obtained from Landauer, Inc., Glenwood, Illinois [5].

1.6 Powered Neutron-Detection Systems: He^3 Proportional Counter

While there are a wide variety of powered neutron detection systems available commercially, the one chosen for evaluation in this project was a He^3 proportional counter. All proportional counters operate under a similar principle. Physically, proportional counters are gas-filled tubes. An incoming ionizing particle, if it has adequate energy, frees electrons from the atomic orbital of the gas atoms, creating ion pairs consisting of an electron and a positively charged atom. The ionizing particle leaves a trail of ion pairs along its trajectory. The electrons then drift towards the anode, or readout electrode, while the positively charged atoms travel toward the cathode. As they drift towards the readout electrode, the electrons gain enough energy to create further ion pairs, which in turn create a cascade of ion pairs known as an avalanche. If the operating voltage of the detector is chosen carefully, each avalanche process occurs independently of other avalanches which derive from the same initial ionizing event. In this way, the total amount of charge created remains proportional to the amount of charge liberated in the original event despite an exponential increase of free electrons. Since the number of ion pairs created by the incident ionizing charged particle is proportional to its energy, one can find the particle's kinetic energy by measuring the total charge between the electrodes. This project uses the Thermo Scientific InterceptorTM(see Figure 1.4 on the following page), a state-of-the-art radiation monitor intended to identify both gamma and neutron radiation and warn the user if a radiation level exceeding a user defined threshold is detected [6]. This system contains a He^3 proportional counter which counts thermal neutrons.

1.7 Current Detection Methods Based on Integrated Circuit Components

While radiation detection methods based on integrated circuit components have been utilized in the past, this class of particle detector has low sensitivity to neutrons. As a result, no neutron-detection system relying on memory cells is currently competitive with other detectors. Conventional detection systems that rely on integrated circuit components are the direct ion storage



Figure 1.4: Thermo Scientific InterceptorTM.

(DIS) dosimeter and the metal oxide semiconductor field effect transistor (MOSFET) dosimeter. The DIS dosimeter pairs a gas-filled ion chamber with a semiconductor nonvolatile memory cell. The MOSFET dosimeter has been used to measure cumulative exposure to ionizing radiation. Both of these detectors have been used to effectively measure X- and gamma rays [2]. The MOSFET dosimeter has been shown to detect fast neutrons through the use of an adjacent hydrogenous converter layer that generates recoil protons, but is relatively insensitive compared to other methods [2].

Chapter 2

Utilizing Static Random Access Memories for Neutron Detection

While Chapter 1 focused on conventional neutron-detection systems, this chapter outlines the development of a new concepts in neutron detection. Specifically, it focuses on the mechanism that makes the development of a memory-based neutron-detection system possible. In addition, it outlines the modification process that was used to enhance the memory chips' sensitivity to radiation.

2.1 Related Work: Perforated Thin Film Coated Semiconductor Thermal Neutron Detectors

Before the detailed discussion regarding the use of SRAMs and neutron detectors, it is worth mentioning research related to the neutron detection concept evaluated by this project. Currently, research led by Douglas S. McGregor is being conducted at Kansas State University that focuses on the development of a perforated and thin film coated semiconductor thermal neutron detector. The detectors are pin diodes that are produced from high purity Si wafers that have thousands of circular perforations etched vertically into the surface of the wafer. These perforations are then backfilled with neutron

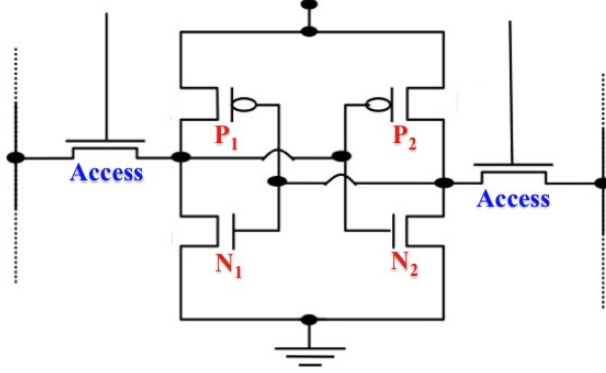


Figure 2.1: Six-transistor SRAM schematic [9]. Two n-type (N1 and N2) and two p-type (P1 and P2) transistors form two cross-coupled inverters that store a single bit of information (a binary 0 or 1). The two transistors labelled “Access” are used during read and write operations.

converter materials, namely B^{10} and/or Li^6 . Prototype devices delivered over 3.8% thermal neutron detection efficiency while operating on 15 V. Higher efficiencies (greater than 30%) are listed for similar devices, however these efficiencies are based on modeling rather than experimental results and the voltage/power requirements are not given. Due to the compact size, relatively low power requirements and low cost of production, these devices could feasibly be implemented for both dosimetry and remote monitoring [7][8].

2.2 Static Random Access Memory Device Layout

Figure 2.1 shows a single memory storage location of a typical static random access memory (SRAM). Each bit in an SRAM is stored on four transistors (two n-type, N1 and N2, and two p-type, P1 and P2) that form two cross-coupled inverters. This storage cell has two stable states which are used to denote binary 0 and 1. Two additional access transistors control the access to a storage cell during read and write operations. A typical SRAM, therefore, uses six transistors to store each memory bit.

2.3 Soft Error Phenomenon and Single Event Upsets

Errors in electronics are typically divided into two categories, hard and soft. Hard-errors are caused by defects—usually due to mistakes in design or construction, or a broken component. They are permanent, irreversible errors. Soft-errors, on the other hand, involve the spontaneous change in the digital information in a memory cell without damage to the component. Soft errors involve changes to data but not changes to the physical circuit itself.

In an SRAM, a soft error involving a change of state caused by ions striking a sensitive node, is called a single event upset (SEU). The mechanism by which an SEU is produced occurs after an energetic ionizing particle has been brought to rest in the silicon near sensitive device nodes (N1, N2, P1, and P2 in Figure 2.1 on the preceding page). As the charged particle traverses through the silicon, it produces a dense radial distribution of electron-hole pairs as illustrated in the the n-type junction shown in Figure 2.2(a) on the next page. If this ionization track traverses the depletion region, “carriers are rapidly collected by the electric field, thereby compensating for the charge stored on the junction” [10]. Outside the depletion region, the non-equilibrium charge distribution creates a temporary funnel-shaped potential distortion (see Figure 2.2(b) on the following page) along the path of the ionizing particle, furthering the effects of charge collection by drift (movement of charge carriers due to the applied electric field) [10]. As the funnel collapses, diffusion (distribution of particles from regions of high concentration to regions of low concentration) dominates the collection process (see Figure 2.2(c) on the next page) until all the excess carriers have been collected, recombined, or diffused away from the junction area [10]. The cumulative collected charge (Q_{coll}), depends on the ionizing particle’s energy, trajectory, the junction structure and type, and the local electrical field. If Q_{coll} exceeds the critical charge required for an upset (Q_{crit}), a SEU occurs. Q_{crit} depends on the node capacitance and voltage, the restoring current provided by feedback, and the time required for the circuit to switch to its opposing data state [10].

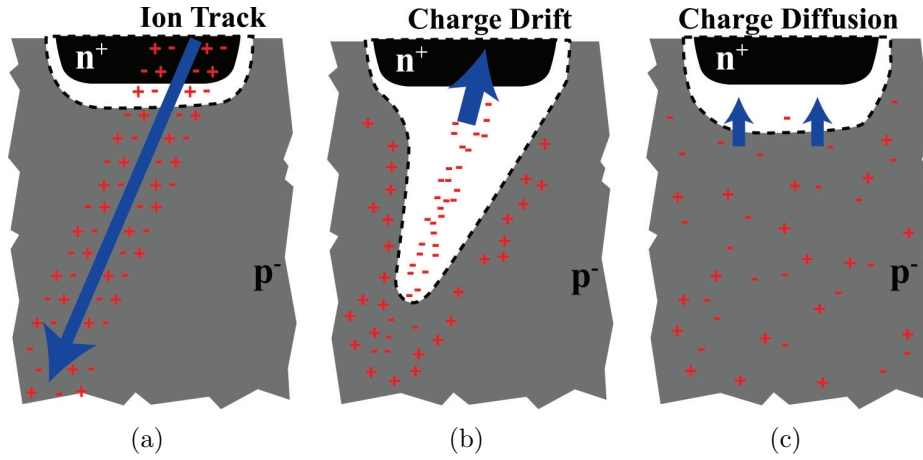


Figure 2.2: Pictorial representation of a single event upset. In 2.2(a), an ionizing particle traverses through a sensitive device node, producing a dense radial distribution of electron-hole pairs. Next, in 2.2(b), the non-equilibrium charge distribution creates a funnel-shaped potential distortion, furthering the effects of charge collection by drift. Finally, as shown in 2.2(c), the funnel collapses, and diffusion dominates the collection process until all the excess carriers have been collected, recombined, or diffused away. If the cumulative charge collected in this process exceeds the critical charge required for a SEU, a bit-flip occurs, indicating the presence of radiation.

2.4 Commercial SRAMs as Neutron Detectors

Analyzing trends in SRAM performance resulting from technological advances is essential to understanding the use of SRAMs in neutron detection. A performance metric useful for this discussion is soft error rate (SER), “which is the sensitivity of a chip to radiation, or its probability of failure from radiation” [11]. SER is of interest because it indicates the probability that a spontaneous change in digital information will result from radiation effects. An SRAM chip with a high SER, therefore, makes an inferior memory device but an excellent neutron detector. (The performance metrics used to evaluate the chips tested in this project are defined in Section 5.1 on page 39).

Remaining valid since originally formulated in 1965, Moore’s Law states that the number of transistors that can be placed inexpensively on an integrated circuit will increase exponentially, doubling approximately every two years [12]. This evolution of integrated circuitry has an important implication: the SER of a common SRAM chip has increased significantly over time. This trend can be explained by considering two important factors: decreased volume of individual bits and the resulting increase in the number of bits/chip. The significantly smaller active volume of the individual transistors results in a decrease in the number of fails/bit (see Figure 2.3 on the next page). As the volume of individual bits decreases, however, the number of bits/chip drastically increases. As a result, the number of soft fails/chip has increased significantly. Although these trends oppose one another, the increased number of bits/chip not only compensates for the decrease in fails/bit, it adds enough bits to reverse the effect and make recent chips more sensitive than older chips. This trend is illustrated in Figure 2.4 on page 16. The resulting implication is that these commercial, off-the-shelf (COTS) chips could prove to be effective neutron detectors.

2.5 Motivation for Sensitivity-Enhancing Modification

Although COTS SRAMs are becoming increasingly more susceptible to radiation-induced SEUs, memory chips are intended to do precisely what their name suggests—store information. For this reason, commercially available chips

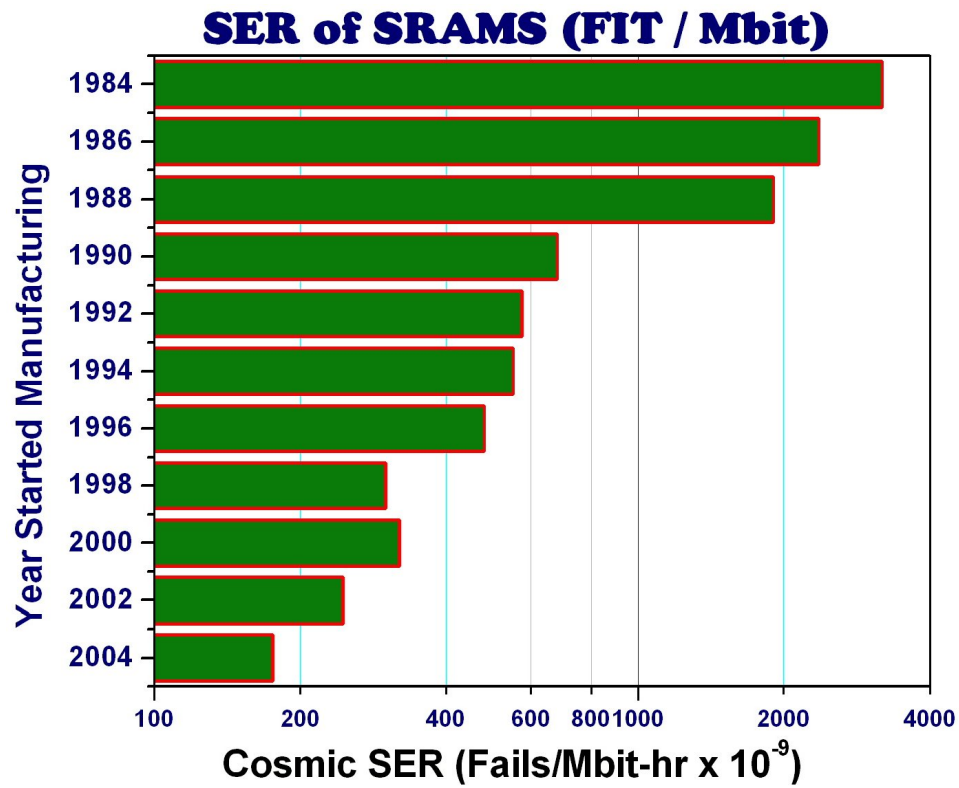


Figure 2.3: SER trends from 1984–2004 [11]. As the active volume of individual transistors decreases over time, there is a decrease in the number of fails/bit.

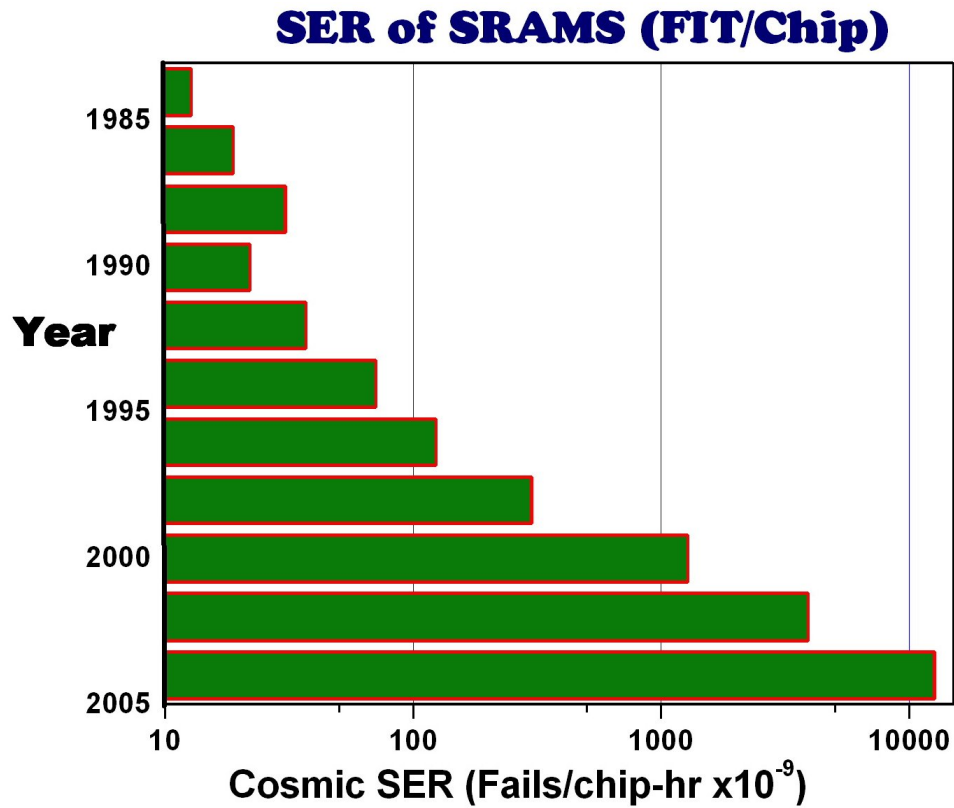


Figure 2.4: SER trends from 1984–2004 [11]. Due to decreasing volume of individual bits, the number of bits/chip drastically increases over time, compensating for the decreased sensitivity of individual bits illustrated in Figure 2.3. Consequently, the number of fails/chip has increased, making the development of a memory-based detection system feasible.

are designed to minimize the effects of radiation. This project aimed to do the opposite in order to fulfill a different purpose: radiation detection. In essence, a forgetful memory makes an excellent neutron detector. Using the phenomenon of soft errors to its advantage, Honeywell 4 MB SRAMS [13] were modified through the removal of a feedback transistor in order to make the devices more susceptible to radiation-induced failures. In addition, a B^{10} conversion layer was applied to increase the chips' susceptibility to SEUs (see Section 2.6).

2.6 Modification Process

2.6.1 Etching Process

The modification of the chip requires three steps: etching, B^{10} deposition, and passivation. The first step, etching, facilitates the use of the neutron-induced $B^{10}(n,\alpha)Li^7$ reaction that greatly enhances the sensitivity of the chips (discussed in detail in Sub-Section 2.6.2 on page 20). In order to successfully develop a process to accomplish the modification, it was decided that two etching processes should be pursued in parallel. At the University of Florida, deep reactive-ion etching (DRIE) was pursued (accomplished by the author while at the University of Florida for an internship during May–June 2009). Concurrently, the Naval Research Laboratory (NRL) examined the feasibility of xenon difluoride (XeF_2) dry etching. Both these etching processes capitalize on a special attribute of the chips—silicon on insulator (SOI) technology. SOI-based devices differ from conventional silicon-built devices in that the silicon junction is above an electrical insulator, silicon dioxide (SiO_2). While the implementation of SOI technology is one of several manufacturing strategies employed to allow the continued miniaturization of microelectronic devices, the technology serves a very different purpose in the context of this project. Both DRIE and XeF_2 dry etching are highly selective processes. This means that they etch through silicon (Si) at a significantly faster rate than SiO_2 . Thus, the etching process essentially stops at the SiO_2 layer, allowing the removal of the silicon substrate without doing damage to the chip's circuitry.

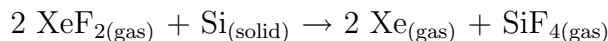
DRIE is a highly anisotropic etch process (i.e. results in nearly vertical walled trenches) used to create deep, steep-sided trenches in silicon. This technique alternates repeatedly between two modes to achieve nearly vertical



Figure 2.5: Chip being mounted on a 4 inch carrier wafer.

structures. The first mode is a standard plasma etch. The plasma contains sulfur hexafluoride (SF_6) that attack the wafer in a nearly vertical direction. In the second mode, a chemically inert passivation layer is deposited. The passivation protects the entire substrate from further chemical attack and prevents further etching. However, during the etching phase, the directional ions that bombard the substrate attack the passivation layer at the bottom of the trench (but not along the sides), exposing the substrate to the chemical etchant [14]. In order to utilize this approach, the chip is mounted on a carrier wafer and masked with Kapton Tape, a film that is highly resistant to the the etchant chemicals (see Figure 2.5). The carrier wafer allows the chip to be inserted in to the DRIE chamber (see Figure 2.6 on the following page). The Kapton Tape serves as a mask, allowing only the exposed area to be etched. Figure 2.7 on the next page shows the chip mounted on the carrier wafer after the etch has been completed and the Kapton Tape removed.

XeF_2 is a dry, isotropic etching process that shows very high selectivity of Si over SiO_2 . The etching process utilizes a simple chemical mechanism. The reaction describing the interaction of the XeF_2 gas with Si is:



The XeF_2 dissociates to xenon (Xe) and fluorine (F) on the surface of the silicon. In the case of silicon etching, F atoms reacts with the Si and it is removed. In this process, photoresist (a light-sensitive material used in



Figure 2.6: Carrier wafer being loaded into deep reactive-ion etching chamber.

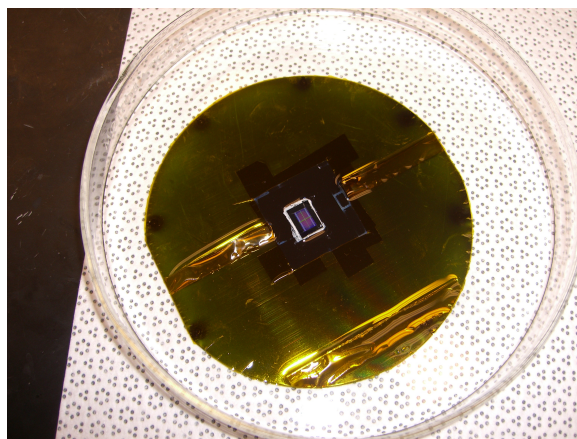


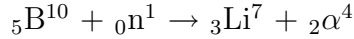
Figure 2.7: Chip after deep reactive-ion etching process has been completed and aperture has been etched.

several industrial processes to form a patterned coating on a surface) is used as a mask.

Both etching techniques, DRIE and XeF_2 dry etching, successfully created apertures in the chips without damaging the memory cells. Ultimately, it was determined that the XeF_2 etching process developed by NRL was preferable because it shows higher selectivity of Si over SiO_2 , allowing the SiO_2 layer to more effectively protect the active circuitry of the chip. In addition, unlike DRIE, the XeF_2 etching process does not require ion bombardment or external energy sources in order to etch silicon.

2.6.2 B^{10} Deposition and Passivation

Neutron-induced reactions that create secondary radiations of adequate energy for direct detection are common in neutron-detection systems. In order to greatly increase the sensitivity of the SRAM chips, they have been modified to exploit the interaction shown below:

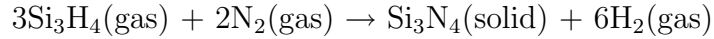


When induced, this neutron interaction releases a lithium and an alpha particle of significant energy in exactly opposite directions. The vast majority of these reactions (94%) leave the Li^7 ion in its first excited state. The Q-value for this reaction is 2.130 MeV and results in reaction products, namely Li^7 and α particles, with energies of 0.840 MeV and 1.470 MeV, respectively. The $2200 \frac{\text{m}}{\text{s}}$ neutron cross-section of this reaction is quite high (3840 b), but drops rapidly with increasing neutron energy and is inversely proportional to neutron velocity. Ideally, for every neutron that hits the sensitivity-enhancing layer of B^{10} , one heavy, charged particle will interact with the SRAM memory cell and cause a soft error. In order for the lithium and alpha particles released by the interaction to cause soft errors, the layer of B^{10} must be applied close to the active memory of the circuit. To accomplish this, all but about 1 μm of the silicon substrate is etched away. Once this material is removed, a thin B^{10} film is deposited in the resulting free space (see Figure 2.8 on page 22). In this way, thermal neutrons hitting the B^{10} release heavy, charged particles that are much more likely to cause soft errors and indicate the presence of neutrons. It is important to note that while the author was at the University of Florida, it was determined that the stress on silicon due to

a B¹⁰ deposition of 3 μm is approximately 800 MPa. The stress is compressive and has the potential to damage the chip's circuitry. This fact directly impacts design decisions as discussed in Section 5.3 on page 41.

Once the chips had been etched using the XeF₂ dry etching process discussed in Sub-Section 2.6.1 on page 17, a 1 – 2 μm layer of B¹⁰ was deposited. To accomplish this, electron beam physical vapor deposition (EBPVD) was used. In EBPVD, a target anode is bombarded with an electron beam given off by a charged tungsten filament under high vacuum. The electron beam causes target atoms to transform into the gaseous phase. Once vaporized, the atoms fill the vacuum chamber and deposit in solid form, coating everything with a thin layer of the target material.

After the B¹⁰ has been deposited, it is necessary to passivate the thin film to prevent it from oxidizing when in contact with air. The material chosen for this purpose is 25 nm layer of silicon nitride (Si₃N₄). As a passivation material, it is superior to SiO₂. It is a significantly better diffusion barrier against water molecules and sodium ions, two major sources of corrosion and instability in microelectronics [15]. This is accomplished by chemical vapor deposition (CVD). CVD can be defined as the deposition of a solid on a heated surface from a chemical reaction in the vapor phase [15]. The chemical reaction for Si₃N₄ deposition is shown below:



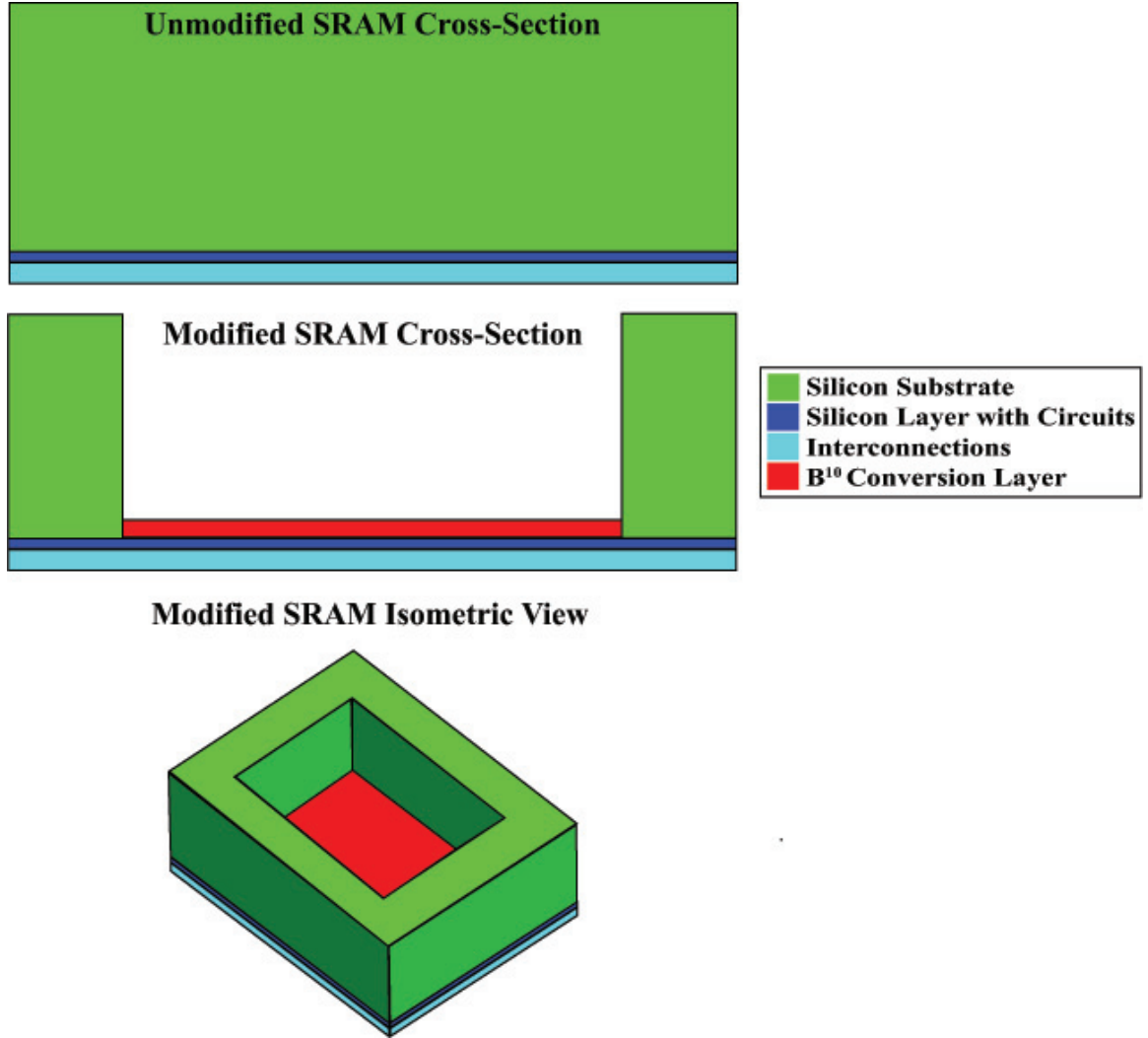


Figure 2.8: Unmodified SRAM cross-section and modified SRAM cross-section and isometric representations. An aperture was etched by removing a portion of the SRAM's silicon substrate so that a B^{10} conversion layer could be applied close to the silicon layer with circuits. This was necessary for the secondary radiations created in the neutron-induced $B^{10}(n,\alpha)Li^7$ reaction to cause SEUs, indicating the presence of radiation.

Chapter 3

Experimental Set-Up at the United States Naval Academy

This chapter provides details about the experimental set-up used at the United States Naval Academy (USNA). First, a functional block diagram that shows all the subsystems and how they interacted will be discussed in Section 3.1. Next, Sections 3.2 through 3.5 will discuss the subsystems in more detail.

3.1 Functional Block Diagram

In order to establish the detection systems' response to radiation, a collection of subsystems was developed as shown in Figure 3.1 on the following page. Table 3.1 on page 25 summarizes additional information regarding the subsystems and their functions and measurement techniques. In order to create a radiation environment suitable for testing the neutron detection systems, neutron sources that provided neutrons of a well defined energy and flux were needed. In this experiment, two neutron sources were used—a plutonium beryllium (PuBe) neutron source and a deuterium-tritium (D-T) neutron generator. Because some of the detection systems (bubble dosimeters, He³ Interceptor[™], and the modified SRAMs) were thermal neutron detection systems, the neutrons emitted by the source needed to be slowed to the thermal energy range. The moderator, specifically sheets of polyethylene, accomplished this function. After passing through the moderator, the neutrons interacted with the array of neutron detection systems. The de-

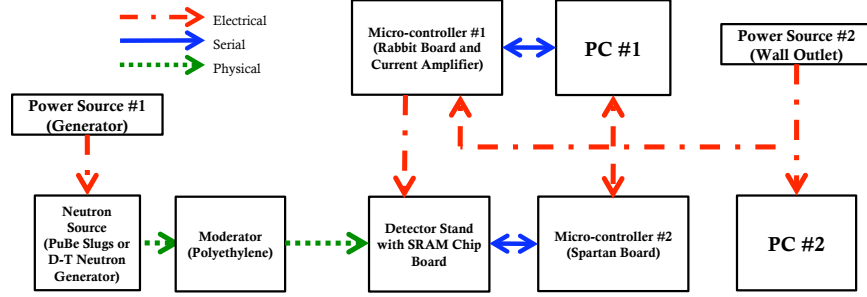


Figure 3.1: Functional block diagram illustrating the experimental set-up required to interrogate the chip.

tection systems were held at the same height and distance from the source by a detector stand. The detector stand included a slot for a chip board that held the various SRAMs, ultimately allowing for their voltage control of and serial communication with the chips. Micro-controller #1 and PC #1 controlled the core operating voltage of the chip, while micro-controller #2 and PC #2 communicated with the chip, writing memory patterns and then reading them after exposure to check for SEUs.

3.2 Neutron Source and Moderator

In order to analyze the detectors' response, neutron sources with different neutron energies and fluxes were used. Neutron flux quantifies the total path-length traveled by the neutrons per unit volume, per unit time. For a mono-directional beam of neutrons, neutron flux becomes the number of neutrons crossing a surface area per unit time. This value is most commonly measured in $\frac{n}{\text{cm}^2 \cdot \text{s}}$. As long as the dynamic range of each detection system is not exceeded, each detector's sensitivity should be independent of the source's flux. In other words, the *percentage* of neutrons the detector is able to detect in a given period of time should not be affected by the total number of neutrons passing through it. In order to establish that this was the case, especially in the analysis of the memory-based detection system, two neutron sources were used. The first source was a stack of five PuBe slugs which emit approximately $10^7 \frac{n}{\text{s}}$ with an average energy of 4 MeV (see Figure 3.2 on page 26). The second is a Thermo-Electron deuterium-tritium (D-T) accelerator (see Figure 3.3 on page 27), which produces 14.3 MeV

Subsystem	Function and Measurement Technique
Neutron Source	Provide neutrons of a well defined energy and flux. Fast flux determined through copper foil activation.
Moderator	Slow neutrons to thermal energy range. Thermal flux determined through indium foil activation.
Detector Stand	Hold array of detectors at equal height and radial distance from source.
Micro-controller #1	Provide user-defined core operating voltage to chip. Monitored with oscilloscope.
PC #1	User interface with micro-controller #1. Compile user input.
Micro-controller #2	Interface between SRAM chip board and PC #2. Read and writes bit pattern to SRAM.
PC #2	Signal processing, user interface with micro-controller #2. Receives, compiles, and prints data from micro-controller #2.

Table 3.1: Subsystems and their functions and measurement techniques.



Figure 3.2: One of five PuBe slugs.

neutrons. Both sources emit neutrons isotropically. All exposures were conducted in Rickover Hall, Room 073 at the United States Naval Academy. As the exposure room is relatively small, significant neutron scattering off the room walls occurred, which affected the fluxes measured for both sources. A schematic of this room is provided in Figure 3.4 on page 28.

Because the primary objective of this project was to determine the thermal neutron detection efficiency and thermal neutron sensitivity of modified SRAMs (see Section 5.1 for definitions of these performance metrics), the neutron sources were moderated with polyethylene to slow a portion of the neutrons to the thermal energy range. To determine what thickness of polyethylene moderator was most appropriate for each of these sources, the thermal neutron flux and cadmium ratio (a measure of how thermalized the neutron source is, see Sub-Section B.1.1 on page 61) were determined. The higher the cadmium ratio, the more thermalized the neutron spectrum. Both the thermal neutron flux and the cadmium ratio were measured through foil activation, a technique discussed in detail in Section B.1 on page 60. The foils were held by the detector stand during exposure, at a radial distance of 46 cm from the source. The foil activation results are summarized in Table 3.2 on page 29 for the PuBe source and Table 3.3 on page 29 for the D-T Neutron Generator. As these results were required only to make a decision about what thickness of polyethylene moderator to use for each source, only one reading was taken at each thickness and no statistical uncertainty for these values was calculated.

For the PuBe slugs, maximizing the thermal neutron flux was important for the practical reason that significant exposure times were required for neutron fluxes of this low magnitude. As shown in Table 3.2 on page 29, the maximum neutron flux of $250 \frac{n}{\text{cm}^2 \cdot \text{s}}$ with the PuBe slugs occurred when 3 in



Figure 3.3: Thermo-Electron 14.3 MeV D-T neutron generator located in Rickover Hall.

of polyethylene was used. For thickness greater than 3 in, the polyethylene acted as a moderator and a shield, absorbing a portion of the neutrons. This accounts for the drop in thermal flux for polyethylene thicknesses greater than 3 in. It should also be noted that contrary to expectations, the cadmium ratio did not consistently increase with greater thicknesses of polyethylene. Hence, it is believed that the cadmium ratios for the polyethylene thicknesses of 9 in and 12 in shown in Table 3.2 are not accurate. Possible sources of error are the software used to measure the induced activity in the foil and the complicated radiation environment created due to the layout and dimensions of the exposure room. However, since these thicknesses of polyethylene were not further used to moderate the PuBe source, this anomaly was not explored further.

For the neutron generator, which provided neutron fluxes significantly higher than the PuBe slugs, exposure times were not a significant issue. Instead, a high cadmium ratio was appropriate because a highly thermalized neutron environment would limit the effects of fast neutrons on the chip. As shown in Table 3.3 on page 29, the highest cadmium ratio available with the neutron generator was with 12 in of polyethylene. Fast neutron

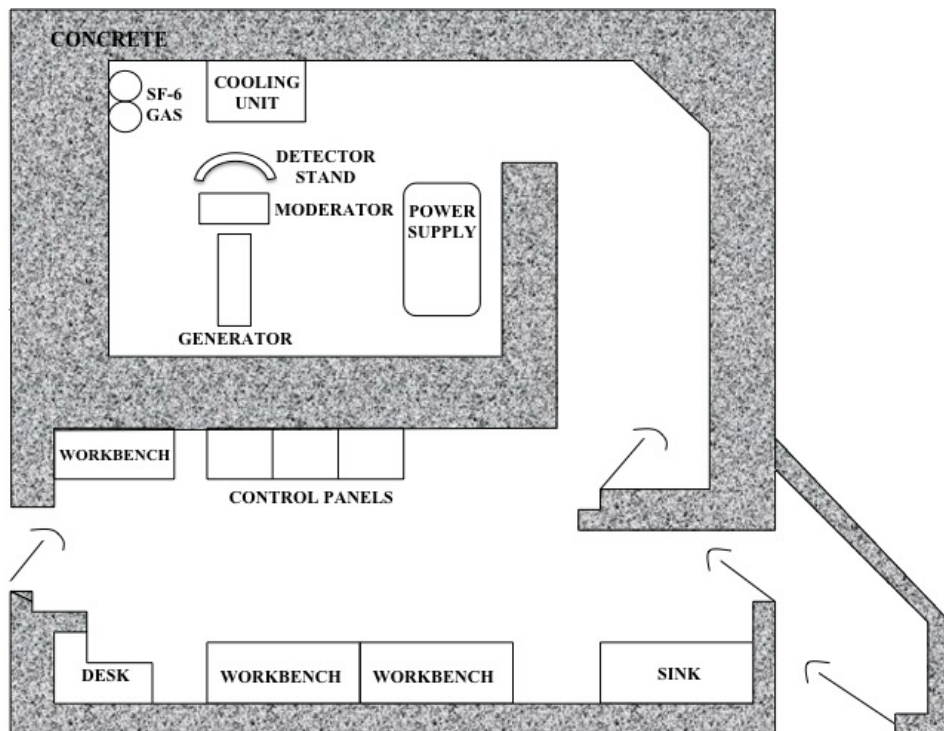


Figure 3.4: Schematic of Rickover 073, the United States Naval Academy's neutron generator room and control room.

Polyethylene Thickness [in]	0	3	6	9	12
Thermal Flux $\left[\frac{n}{\text{cm}^2 \cdot \text{s}} \right]$	60	250	130	90	50
Cadmium Ratio	8	12	17	27	17

Table 3.2: Characterization of the PuBe neutron generator environment with varying polyethylene thicknesses.

Polyethylene [in]	0	3	6	9	12
Fast Flux $\times 10^{-5} \left[\frac{n}{\text{cm}^2 \cdot \text{s}} \right]$	17	8.45	4.2	1.9	0.89
Thermal Flux $\times 10^{-5} \left[\frac{n}{\text{cm}^2 \cdot \text{s}} \right]$	1.2	4.8	3.2	2.6	1.8
Cadmium Ratio	9	10	13	14	16

Table 3.3: Characterization of the 14.3 MeV neutron generator environment with varying polyethylene thicknesses.

fluxes were determined for this source through copper foil activation (see Sub-Section B.1.2 on page 63) in order to establish the unmodified SRAM as a control chip (see Section 5.2 on page 40). The fast flux was inversely proportional to polyethylene thickness since more neutrons were slowed to the thermal range .

3.3 Detector Stand

Both of the neutron sources used in this project were assumed to be isotropic, emitting neutrons uniformly in all directions. For this reason, a stand was needed to hold the array of detection systems analyzed in the project at the same height and distance from the neutron source. A detector stand machined out of aluminum was designed for this purpose. Aluminum was chosen for the stand material because of its relatively small effect on the neutron environment and the thermal neutron flux. Windows were cut out so that the detection systems could be easily mounted and unmounted from the rear, minimizing the amount of time the user would be exposed to radiation during detector change-outs (see Figure 3.5 on the next page). The stand

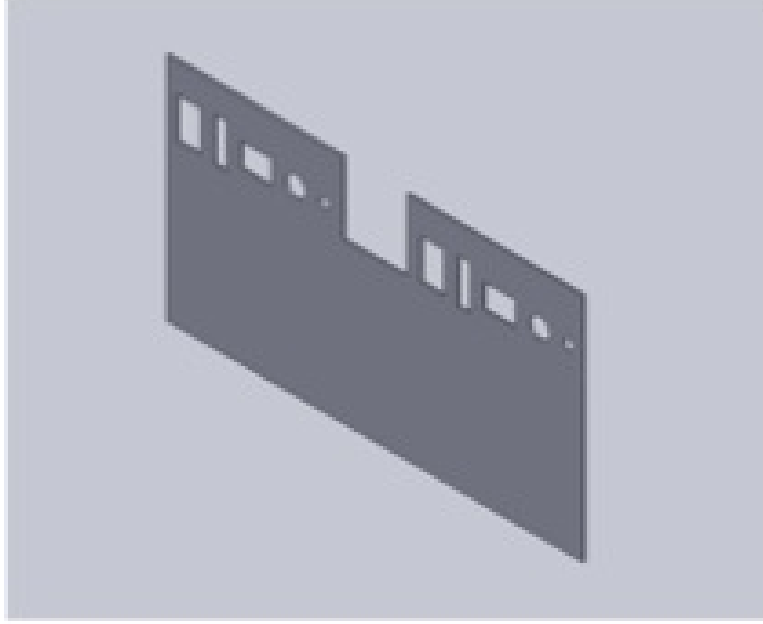


Figure 3.5: Detector stand model shown flat with windows for neutron-detection systems.

was designed to be arc-shaped (see Figures 3.6 on the following page and 3.7 on page 32) with a radius of 46 cm so that when positioned 46 cm from the neutron source, all the neutron-detection systems would be a uniform distance from the source (regardless of the thickness of polyethylene present).

3.4 Micro-Controller #1 and PC #1 (SRAM Core Operating Voltage Control)

An aim of the project was to study the effect of SRAM core operating voltage on neutron detection efficiency and sensitivity. As discussed in Section 2.3 on page 12, in order for an ionizing particle to cause a SEU, the Q_{coll} it induces must be greater than Q_{crit} . Many of the factors that influence these two quantities are not controllable. The chips analyzed in this project, however, have a variable core operating voltage. As a consequence, the node voltage of the chip is adjustable. Lower node voltages result in lower values of Q_{crit}

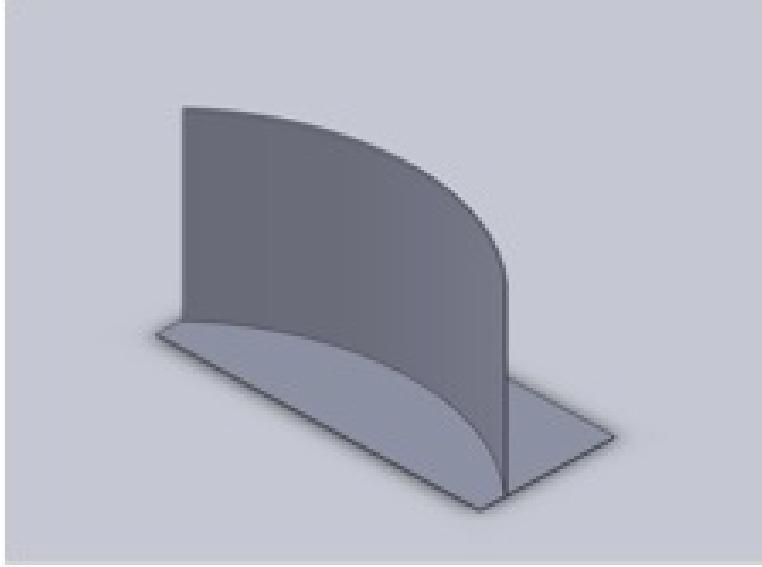


Figure 3.6: Detector stand model shown curved.

and a lower threshold required for a SEU to occur.

In order to precisely control the core operating voltage of the SRAMs tested in this project, a Rabbit 3000 microprocessor was used (micro-controller #1, see Figure 3.8 on page 33). Accompanying software was written in Dynamic C that compiled to the Rabbit board where a built-in digital-to-analog converter supplied requested voltages. PC #1 acted as the user interface with micro-controller #1, allowing for the writing and implementation of core operating voltage control software. There were two important SRAM limitations considered in writing the software. First, the core operating voltage could not dip below about 0.5 V. Second, in order to write to or read the chip, the core operating voltage needed to be near 1.80 V. Violating either of these conditions resulted in the SRAM losing the information stored on the chip and therefore losing information about the radiation environment. With this in mind, the software was designed to transition between user-defined high and low operating voltages by a user defined voltage step. In addition, the user could specify the amount of time the chip would remain at the high and low operating voltages. In this way, the chip could accumulate errors at a reduced operating voltage for a period of time, then the operating voltage could be increased so that the chip could be read. Additionally, a signal con-

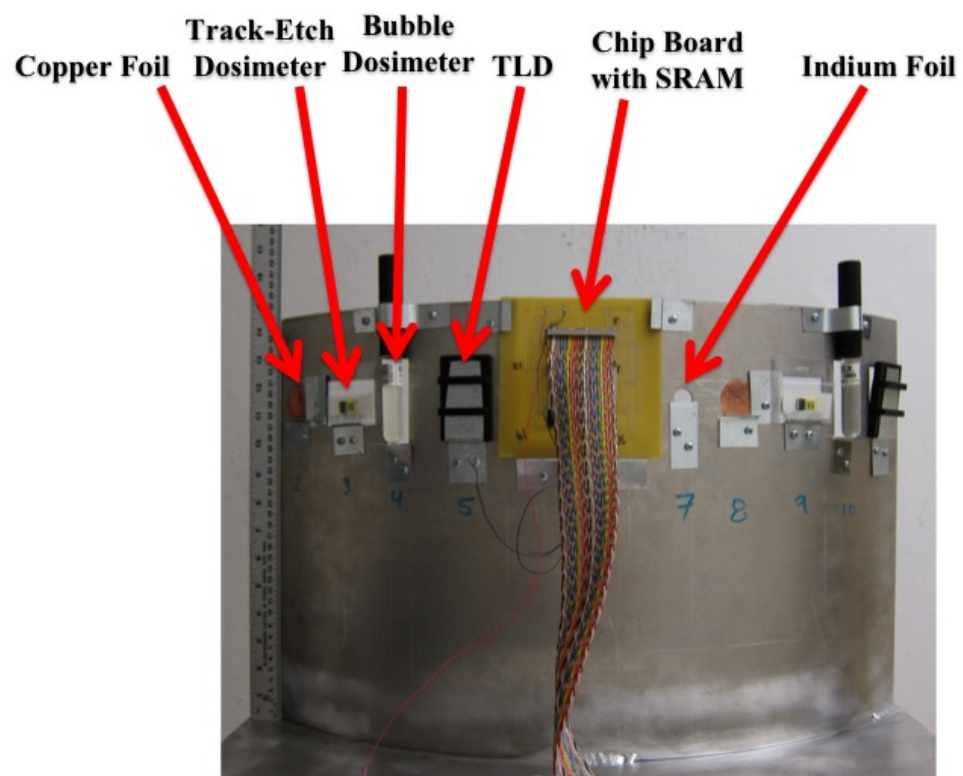


Figure 3.7: Detector stand fabricated by the United States Naval Academy Project Support Branch supporting neutron-detection systems.

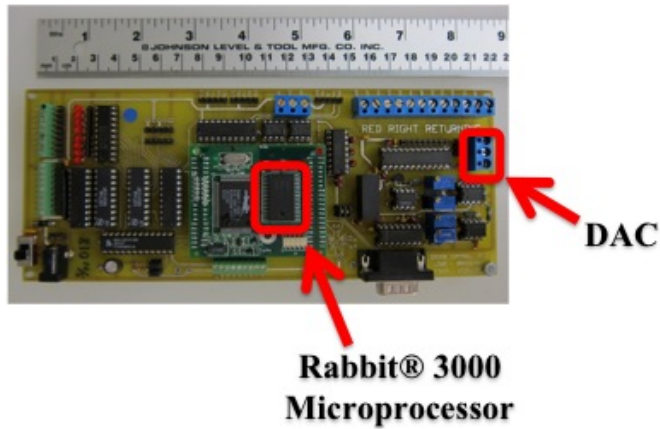
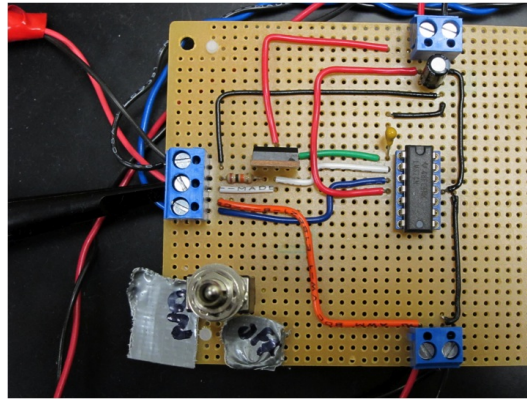


Figure 3.8: Rabbit 3000 microprocessor and supporting hardware developed by the United States Naval Academy Technical Support Department. Software was compiled to microprocessor and the digital-to-analog converter (DAC) sent requested voltages to the SRAMs.

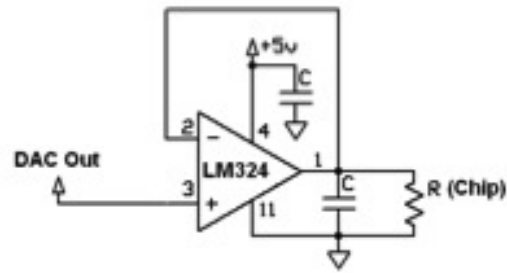
ditioning circuit was designed and built to supplement the current available from the Rabbit board's digital-to-analog converter (see Figure 3.9 on the following page).

3.5 Micro-Controller #2 and PC #2 (Method for Evaluation of SRAM Sensitivity)

In order to establish the sensitivity of an SRAM chip to radiation, a tester that identifies soft errors was utilized. A Xilinx Spartan-3 board was used for this purpose (micro-controller #2 see Figure 3.10 on page 35), communicating serially with the chip and a laptop PC running accompanying MSDOS-based software written in 2004 as part of MIDN Stephan Koev's Capstone Project [16]. The tester loaded a predetermined bit pattern on the chip (a checkerboard of binary 0's and 1's) and interrogated it, checking each time for bit flips indicating the presence of radiation. After each user-prompted interrogation, the tester output the number of SEUs.



(a)



(b)

Figure 3.9: Current amplifier for micro-controller #1. Signal conditioning circuit amplified current available from the micro-controller's digital-to-analog converter (3.9(a)). 3.9(b) shows a schematic for the amplifier.

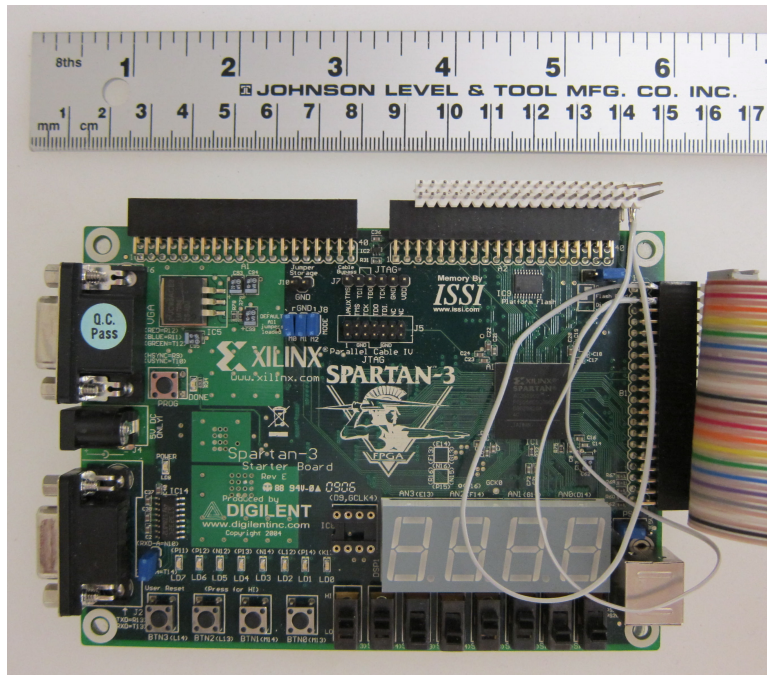


Figure 3.10: Xilinx Spartan-3 microprocessor. Tester identified SEUs by writing a user-defined memory pattern to the SRAM, interrogating it, and checking it for bit flips.

Chapter 4

He³ Interceptor™ Evaluation: Performance Metric and Results

This chapter will discuss the results obtained from the conventional neutron-detection systems. Section 4.1 discusses why the comparison focuses on the Thermo Scientific He³ Interceptor™ system. Sections 4.2 and 4.3 will discuss the performance metric used and results obtained through the evaluation of the Interceptor™.

4.1 Detector Output and Appropriateness of Comparisons

Because each of the five detection systems considered in this project operates utilizing very different mechanisms, their outputs are different. The three non-powered detection systems are designed for dosimetry purposes. This means that they are intended to provide information about neutron dose equivalent. While in the case of the bubble dosimeters and track-etch dosimeters the raw data can be used to calculate a neutron detection efficiency, they are inherently disadvantaged without the conversion factors and algorithms that convert their outputs into neutron dose equivalents. This being the case, the non-powered detection systems designed for dosimetry purposes do not provide good comparisons with the SRAMs. For this reason, this report focuses on the powered detection considered for comparison,

the He³ InterceptorTM. The results obtained for the non-powered systems are included in Section A.2. In the case of the Thermo Scientific He³ InterceptorTM, the detector provided a thermal neutron detection rate in units of $\frac{n}{s}$. By dividing the InterceptorTM's thermal neutron detection rate by the thermal neutron flux and the cross-sectional area of the He³-filled tube, a thermal neutron efficiency was calculated. This quantity is defined in Section 4.2.

4.2 He³ InterceptorTM Performance Metric

For the purpose of this report, thermal neutron detection efficiency (η) is a dimensionless decimal fraction. η for the He³ InterceptorTM is defined as follows:

$$\eta_{\text{He}^3} = \frac{R}{(\phi_{\text{thermal}})(A_{\text{tube}})}, \quad (4.1)$$

where:

$$\begin{aligned} R &= \text{thermal neutron detection rate in counts (n) per second [cps]} \\ \phi_{\text{thermal}} &= \text{thermal neutron flux} \left[\frac{n}{\text{cm}^2 \cdot \text{s}} \right] \\ A_{\text{tube}} &= \text{cross-sectional area of He}^3 \text{ tube in Interceptor}^{\text{TM}} (8.58 \text{ cm}^2 [6]) \end{aligned}$$

4.3 He³ InterceptorTM Results

Because of the sensitive electronic suite housed in the InterceptorTM, it was only exposed to the PuBe source. Since η_{He^3} is normalized by thermal neutron flux, it was not necessary to expose it to the D-T neutron generator in order to compare its neutron detection efficiency to the SRAM's. The intense radiation environment created by the D-T neutron generator was found to quickly saturate the detector and could have potentially destroyed it. During its exposure to the PuBe source (moderated by 3 in of polyethylene), the He³ InterceptorTM was connected to a PC located in the generator control room by an extended USB cable. This allowed for real time monitoring of the detector's response. After the detection system collected sufficient data, the thermal neutron detection rate data was downloaded from the He³ InterceptorTM and imported into MATLAB for analysis. A histogram of the data collected is shown in Figure 4.1 on the next page. The data followed a

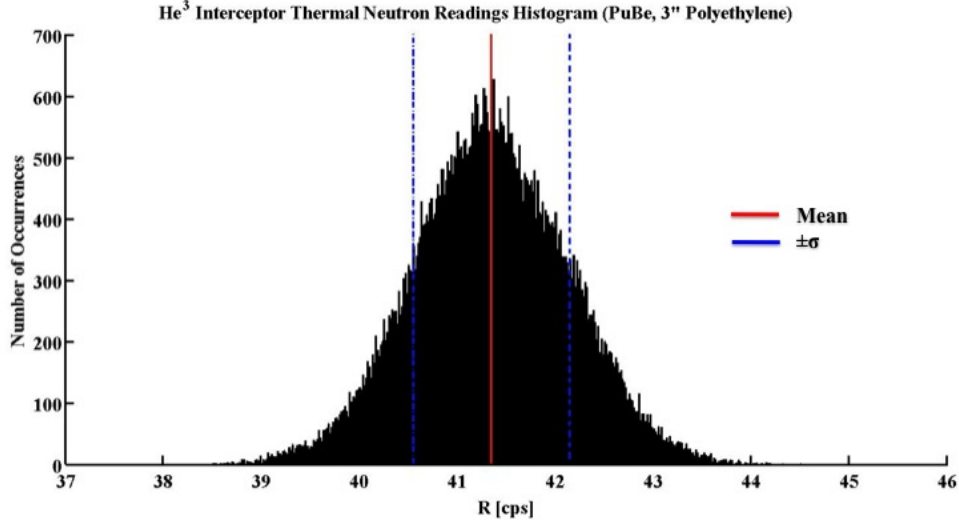


Figure 4.1: Histogram of He^3 InterceptorTM data collected when exposed to PuBe with 3 in of polyethylene moderator. Data followed a normal distribution.

normal distribution. The vertical center line represents the mean of the data and the vertical lines to the right and left represent one standard of deviation below and above the mean. From this data it was determined that η_{He^3} was 0.020 ± 0.010 , where the uncertainty accounts for the nominal 20% uncertainty on thermal neutron detection rates provided by the manufacturer [6], and statistical variation in the thermal neutron detection rate data and the thermal neutron flux data.

Chapter 5

SRAM Evaluation: Performance Metrics and Results

This chapter details the various characterizations performed for the memory-based detection system this project sought to analyze. First, in Section 5.1 the performance metrics used will be discussed. Sections 5.2 and 5.3 will establish the use of unmodified chips and controls as well as outline the various chip designs tested. Finally, Section 5.4 will present the results obtained by the project.

5.1 SRAM Performance Metrics

In evaluating the performance of the modified SRAM detectors, two performance metrics were used. The first metric is thermal neutron detection *efficiency*. For the purpose of this report, thermal neutron detection efficiency (η) is a dimensionless decimal fraction that is the ratio between the number of neutrons detected and the number of neutrons that passed through the aperture of the SRAM during a finite period of time. For the SRAMs, neutron detection efficiency is defined as follows:

$$\eta_{\text{SRAM}} = \frac{N_{\text{SEU}}}{(\phi_{\text{thermal}})(A_{\text{aperture}})(t_e)}, \quad (5.1)$$

where:

$$\begin{aligned}
N_{\text{SEU}} &= \text{number of SEUs the SRAM suffers during a given exposure} \\
\phi_{\text{thermal}} &= \text{thermal neutron flux } \left[\frac{\text{n}}{\text{cm}^2 \cdot \text{s}} \right] \\
A_{\text{aperture}} &= \text{aperture area } [\text{cm}^2] \\
t_e &= \text{length of exposure } [\text{s}]
\end{aligned}$$

The second metric is thermal neutron *sensitivity*. Neutron sensitivity (S) is a measure of the number of fails per unit neutron fluence in units of $\frac{\text{SEU}}{\frac{\text{n}}{\text{cm}^2}}$. Neutron fluence is defined as the neutron flux integrated with respect to time and represents the total neutron path-length per unit volume. For mono-directional sources, like the ones used in this project, this becomes the total neutron path-length per unit area. S is defined as follows:

$$S = \frac{N_{\text{SEU}}}{(\phi_{\text{thermal}})(t_e)}, \quad (5.2)$$

where:

$$\begin{aligned}
N_{\text{SEU}} &= \text{number of SEUs the SRAM suffers during a given exposure} \\
\phi_{\text{thermal}} &= \text{thermal neutron flux } \left[\frac{\text{n}}{\text{cm}^2 \cdot \text{s}} \right] \\
t_e &= \text{length of exposure } [\text{s}]
\end{aligned}$$

While similar conclusions can be drawn from these metrics, their fundamental differences are important—especially when it comes to future design considerations. This project showed that thickness of the B^{10} conversion layer and the core operating voltage of the chip influences neutron detection efficiency. Unlike neutron detection efficiency, the aperture area strongly influences neutron sensitivity. Distinguishing between these two performance metrics is important when making statements about future generations of this memory-based detection system. This distinction will be discussed in Sub-Section 5.4.4 on page 49 and Section 6.3 on page 54.

5.2 Unmodified SRAM as a Control

The modified SRAMs are designed to utilize the $\text{B}^{10}(\text{n},\alpha)\text{Li}^7$ reaction, which has a high probability of occurring when the energy of incident neutrons are

in the thermal range (see Sub-Section 2.6.2 on page 20). For this reason, the modified SRAMs are designed to be thermal neutron detectors. SRAMs can suffer some errors, however, due to interactions between high-energy neutrons and the memory cells. As a consequence, in order to make statements about the modified SRAM’s thermal neutron detection potential—the function for which they were designed—there must be a correction factor applied to the modified SRAM data in order to disregard the influence of high-energy neutrons. The unmodified SRAM, which does not have the advantage of a B^{10} conversion layer, facilitates this distinction. While it did suffer a small number of errors during exposures, these errors are due to neutrons outside the thermal energy range [9]. The number of errors the unmodified chip suffered were subtracted from the errors the modified chip suffered in order to determine how many errors were induced by thermal neutrons. In this way, the unmodified SRAM ultimately served as a control chip, allowing for determination of the modified SRAMs’ thermal neutron detection capabilities.

5.3 Modified SRAM Design Considerations and Specifications

The first generation of chips modified for this project were designed to optimize neutron detection efficiency. Thus, the most important design consideration was the thickness of the B^{10} conversion layer. Because using SRAMs as neutron detectors is a novel concept, data for other semiconductor-based neutron-detection systems that utilize the $B^{10}(n,\alpha)Li^7$ reaction was used to predict what thickness of B^{10} would optimize neutron detection efficiency (i.e. optimize the relationship between probability of interaction and self-absorption effects within the conversion layer). Research on diode-based detection systems suggests that the optimum film thickness of B^{10} for semiconductor-based neutron detectors is $2.4\text{ }\mu\text{m}$ [17]. Based on the assumption that a layer of B^{10} thickness of about $2.4\text{ }\mu\text{m}$ would maximize neutron detection efficiency in SRAMs and the potential issue of the film inducing damaging compressive stress on the SRAMs’ active circuitry, a relatively small aperture area was chosen for the first generation of chips. These SRAMs have B^{10} conversion layers of varying thicknesses, allowing for a characterization of how the B^{10} thickness actually effected efficiency. While optimizing neutron detection efficiency was desirable, limitation of the aperture area and

SRAM Chip	Aperture Area [cm ²]	B ¹⁰ Thickness [μm]
Control Chip	0.216	Not Applicable
B ¹⁰ Chip #1	0.216	1.4 ± 0.1
B ¹⁰ Chip #2	0.216	1.7 ± 0.1
B ¹⁰ Chip #3	0.216	2.0 ± 0.5
B ¹⁰ Chip #4	0.420	1.0 ± 0.5

Table 5.1: Labels and specifications of chips evaluated in project. The Control Chip was etched but no B¹⁰ was deposited in the resulting free space. B¹⁰ Chips #1–#3 all had small apertures with B¹⁰ thicknesses ranging from 1.4 – 2.0 μm. A relatively small aperture was chosen for these thicknesses of B¹⁰ due to concern about the stress induced on the active circuitry by the B¹⁰ films. B¹⁰ Chip #4 had a larger aperture facilitated by its relatively thin B¹⁰ film.

ultimately neutron sensitivity (defined in Equation 5.2 on page 40) resulted in chips designed to have a larger aperture area. Due to the stress concerns previously discussed, larger apertures required thinner B¹⁰ films. To simplify the discussion of the SRAMs’ performance, the two modified chips studied in this project are referred to as B¹⁰ Chips #1, #2, #3, and #4. The design characteristics of each are given in Table 5.1. The uncertainties provided for the B¹⁰ thicknesses were provided by NRL for B¹⁰ Chips #1 and #2 and by the University of Florida for B¹⁰ Chips #3 and #4. The uncertainties differ because different EBPVD systems were used to deposit the B¹⁰ films.

5.4 Modified SRAM Results

This section summarizes the results obtained for the SRAM-based detection system evaluated in this project. It should be noted that uncertainties presented throughout are purely statistical and represent the standard deviation of the mean, or the standard deviation divided by the square-root of the number of observances.

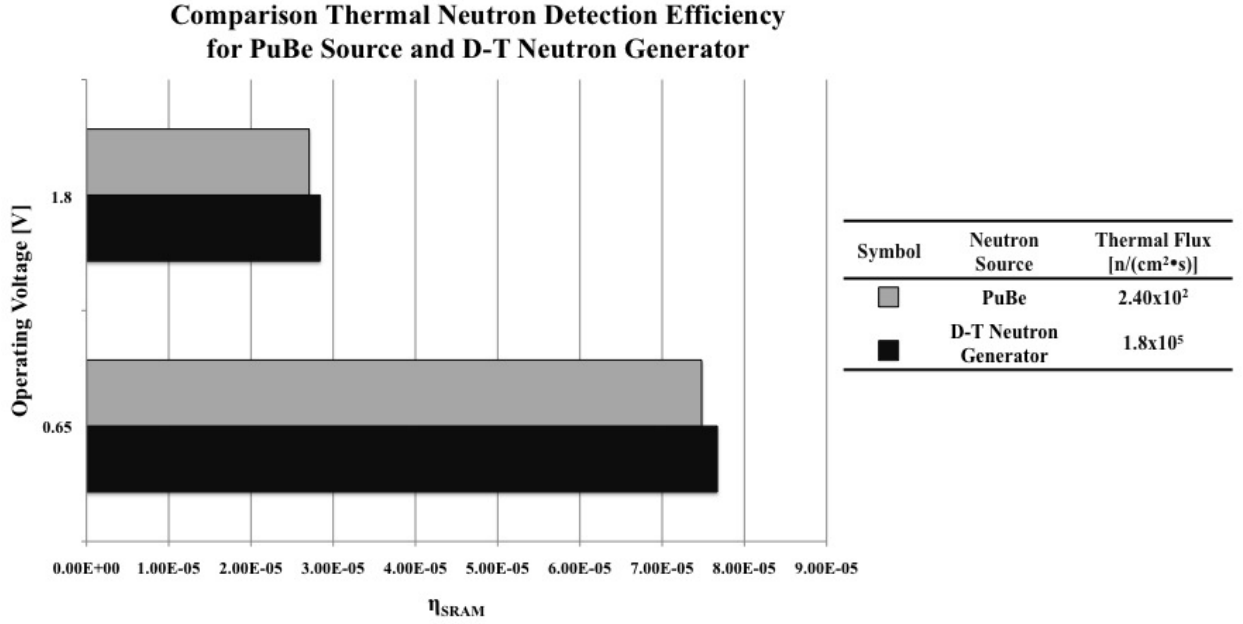


Figure 5.1: Thermal neutron detection sensitivities of B¹⁰ Chip #2 when exposed to PuBe and 14.3 MeV D-T neutron generator. Figure illustrates that η_{SRAM} and S were independent of the source's thermal neutron flux.

5.4.1 Thermal Flux Dependence

As discussed in Section 3.2 on page 24, the SRAM's η and S should be independent of the source's thermal neutron flux. Figure 5.1 and Table 5.2 on the following page show the 0.65 V and 1.80 V thermal neutron detection sensitivities of a modified SRAM when exposed to $240 \pm 10 \frac{\text{n}}{\text{cm}^2 \cdot \text{s}}$ PuBe slugs and the $1.8 \times 10^5 \pm 0.2 \times 10^5 \frac{\text{n}}{\text{cm}^2 \cdot \text{s}}$ D-T neutron generator. As Figure 5.1 illustrates, there was no appreciable difference between the chip's neutron detection efficiencies when exposed to these two sources. With this established, it was decided that additional data would be collected with the D-T neutron generator since the higher thermal neutron flux facilitated shorter exposure times and higher SEU rates.

Core Voltage [V]	$S \times 10^5 \left[\frac{\text{SEU}}{\text{n}} \frac{1}{\text{cm}^2} \right]$	
	PuBe Slugs	Neutron Generator
0.65	1.6 ± 0.1	1.66 ± 0.09
1.80	0.59 ± 0.05	0.61 ± 0.06

Table 5.2: Thermal neutron sensitivities (S) of B¹⁰ Chip#3 when exposed to PuBe and 14.3 MeV D-T neutron generator multiplied by 10⁵. Values illustrate that η_{SRAM} and S were independent of the source’s thermal neutron flux.

B ¹⁰ Chip #	Linear Regression R ² Value	Logarithmic Regression R ² Value
1	0.98	1.00
2	0.97	0.99
3	0.98	1.00
4	0.97	1.00

Table 5.3: R² values for linear and logarithmic regression analysis of core operating voltage dependence.

5.4.2 Core Operating Voltage Dependence

While lower core operating voltages were expected to lower Q_{crit} and therefore result in increased η and S (see Section 3.4 on page 30), it was not known how these quantities would scale with reduced operating voltages. In order to establish the relationship, the SRAMs were tested at various core operating voltages so that the values for η at each voltage could be compared. Figure 5.2 on the next page and Figure 5.3 on page 46 show the regression analyses performed. The coefficient of determination (R²) values of these regressions are summarized in Table 5.3. Values of R² range from 0–1 and an R² value of 1 indicates that the regression line perfectly fits the data. As indicated in Table 5.3, the exponential regression better fits the data. Thus, it was concluded that the neutron detection efficiency scales logarithmically with core operating voltage.

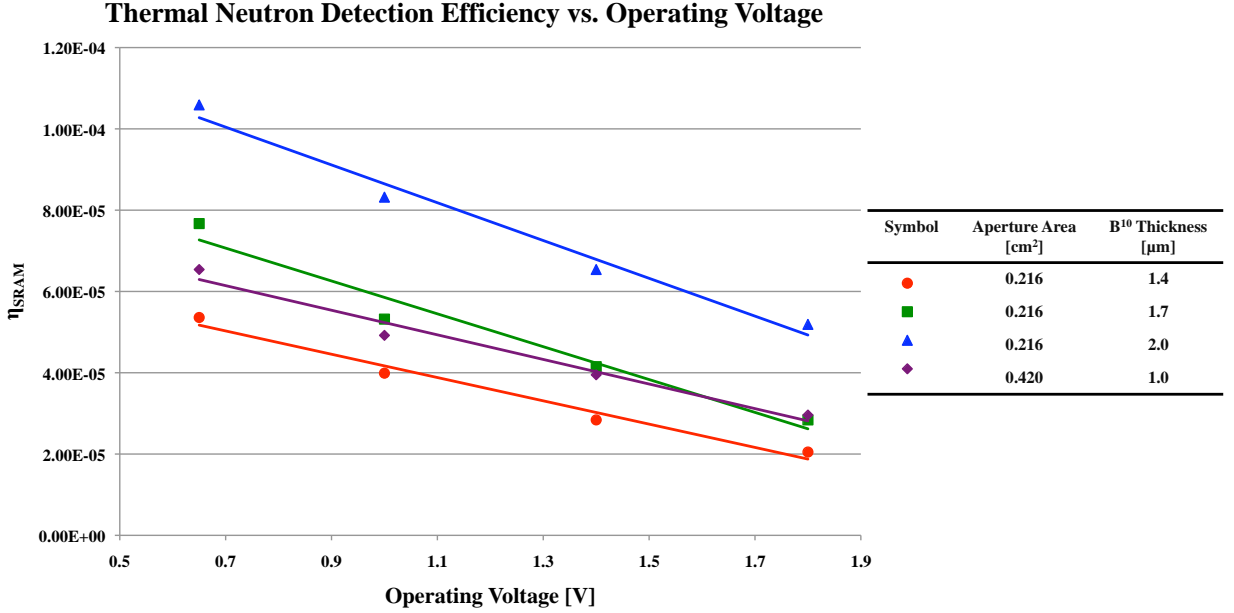


Figure 5.2: Linear regression analysis of core operating voltage dependence.

5.4.3 B¹⁰ Conversion Layer Thickness Dependence

When the neutron mean free path is much greater than the B¹⁰ conversion layer thickness, the B¹⁰ conversion layer thickness is directly proportional to the probability that the B¹⁰(n,α)Li⁷ reaction will occur. While a high probability of interaction between incident neutrons and B¹⁰ is desired, the secondary radiation (Li⁷ and α particles) must reach the active circuitry of the SRAM and deposit enough energy to result in a Q_{coll} greater than Q_{crit} for a SEU to occur. As a consequence, the B¹⁰ thickness must be optimized to balance the probability of interaction with the energy loss the secondary radiation suffers in matter. In order to illustrate these competing factors, a simplified modeling analysis was conducted using “SRIM,” software developed by Dr. J.F. Ziegler, that provides information about the stopping and range of ions in matter [18]. Figure 5.4 on page 47 shows the cross-section of a modified SRAM and defines the locations where secondary radiation particle energies were calculated. The thickness of the SiO₂ and Si layers were taken to each have thickness of 0.15 μm [19]. The calculations summarized in Table 5.4 on page 47 assume that the B¹⁰(n,α)Li⁷ interaction takes place

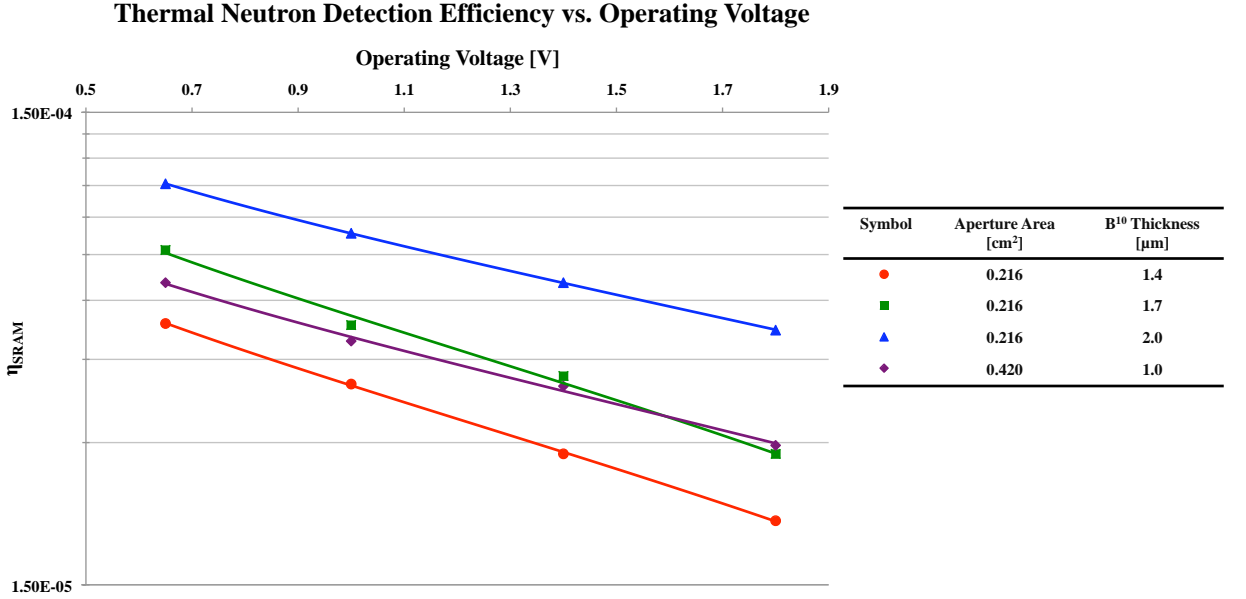


Figure 5.3: Logarithmic regression analysis of core operating voltage dependence.

within the first atom layer of the B¹⁰ conversion layer and the secondary radiation in question recoils perpendicular to the surface towards the SiO₂ and Si layers. E₁, E₂, and E₃ represent the energies of the α or Li⁷ ions at the start of each layer as shown. As shown in Table 5.4 on the next page a B¹⁰ thickness of 2 μm will stop the Li⁷ particle (i.e. its energy goes to zero) while a B¹⁰ thickness of 1 μm will result in the deposition of only 0.024 MeV from the Li⁷ particle. The α particles, on the other hand, deposit [0.045 MeV–0.050 MeV]. Based on the value of Q_{crit} for the SRAMs used in this project, this means that an overwhelming majority of the SEUs are caused by α particles[9] [20]. As a consequence, for the chips analyzed in this project, η_{SRAM} should increase with increased B¹⁰ thickness as a thickness of 2 μm does not result in a significant increase in α particle energy depletion before reaching the Si layer where the active circuitry is located.

Figure 5.5 on page 48 shows η_{SRAM} of B¹⁰ Chips #1, #2, and #3 vs. B¹⁰ thickness at various operating voltages. As expected, η_{SRAM} scaled exponentially with B¹⁰ conversion layer thickness at all voltages.

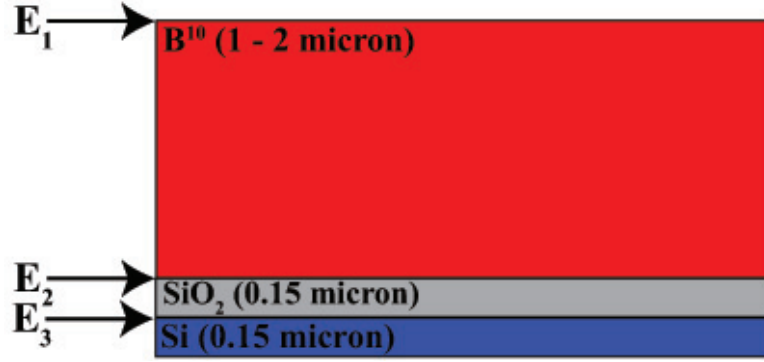


Figure 5.4: Cross-section of modified SRAMS with layer thicknesses. E_1 , E_2 , and E_3 represent the energies of the α or Li^7 ions at the start of each layer as shown.

Particle Energy [MeV]	1 μm B^{10}		2 μm B^{10}	
	Li^7	α	Li^7	α
E_1	0.84	1.47	0.084	1.47
E_2	0.091	1.082	0.0	0.694
E_3	0.059	1.024	0.0	0.633
Energy Deposited in Si	0.024	0.045	0.0	0.050

Table 5.4: Secondary radiation (Li^7 and α) energies at layer boundaries and energy deposited in active circuitry (Si) of modified SRAMs with 2 μm and 1 μm thick B^{10} conversion layers when the $\text{B}^{10}(\text{n},\alpha)\text{Li}^7$ interaction takes place within the first atom layer of the B^{10} conversion layer and the secondary radiation in question recoils perpendicular to the surface towards the Si layer.

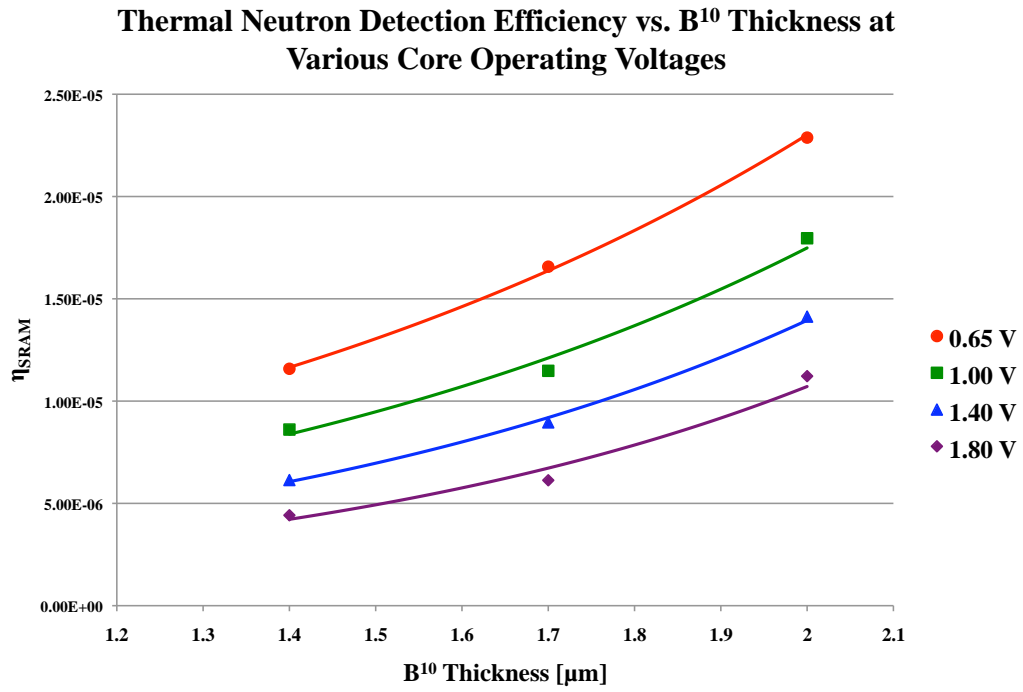


Figure 5.5: η_{SRAM} of B¹⁰ Chips #1, #2, and #3 vs. B¹⁰ thickness at various operating voltages. Figure illustrates that η_{SRAM} was directly proportional to and scaled exponentially with B¹⁰ conversion layer thickness

Core Voltage [V]	$\eta_{\text{SRAM}} \times 10^4 (\text{decimal fraction})$			
	B ¹⁰ Chip #1	B ¹⁰ Chip #2	B ¹⁰ Chip #3	B ¹⁰ Chip #4
0.65	0.54 ± 0.04	0.77 ± 0.04	1.06 ± 0.08	0.65 ± 0.04
1.00	0.40 ± 0.02	0.53 ± 0.03	0.83 ± 0.06	0.49 ± 0.03
1.40	0.28 ± 0.02	0.42 ± 0.02	0.65 ± 0.02	0.40 ± 0.02
1.80	0.21 ± 0.01	0.28 ± 0.03	0.52 ± 0.03	0.30 ± 0.02

Table 5.5: η_{SRAM} of B¹⁰ Chips #1–#4 at various core operating voltages. Values illustrate that B¹⁰ Chip #3 was the most efficient at every core operating voltage tested.

5.4.4 Thermal Neutron Detection Efficiency vs. Thermal Neutron Sensitivity

In comparing the modified SRAMs, it is important to consider both η and S . Considering these two performance metrics illuminates important ideas about design considerations. Figure 5.6 on the next page and Table 5.5 summarize η for B¹⁰ Chips #1–#4. B¹⁰ Chip #3 was more efficient than the others at every core operating voltage tested. This is due to the fact that η is normalized by the aperture area of the chips, giving B¹⁰ Chip #3 an advantage due to its greater B¹⁰ thickness. The greater B¹⁰ thickness increases the probability that an incident neutron will undergo the B¹⁰(n, α)Li⁷ reaction.

While B¹⁰ Chip #3 proved to be the most efficient, potential stress effects in B¹⁰ Chip #3 resulted in a desire for a thinner B¹⁰ film. In order to compensate for the decreased efficiency, the aperture area of B¹⁰ Chip #4 was increased. Figure 5.7 and Table 5.6 on the next page summarize S for B¹⁰ Chips #1–#4. B¹⁰ Chip #4 was the most sensitive at every core operating voltage tested. These results illustrate the fact that sacrificing efficiency in order to allow for larger aperture areas results in a more sensitive and therefore more effective thermal neutron detector.

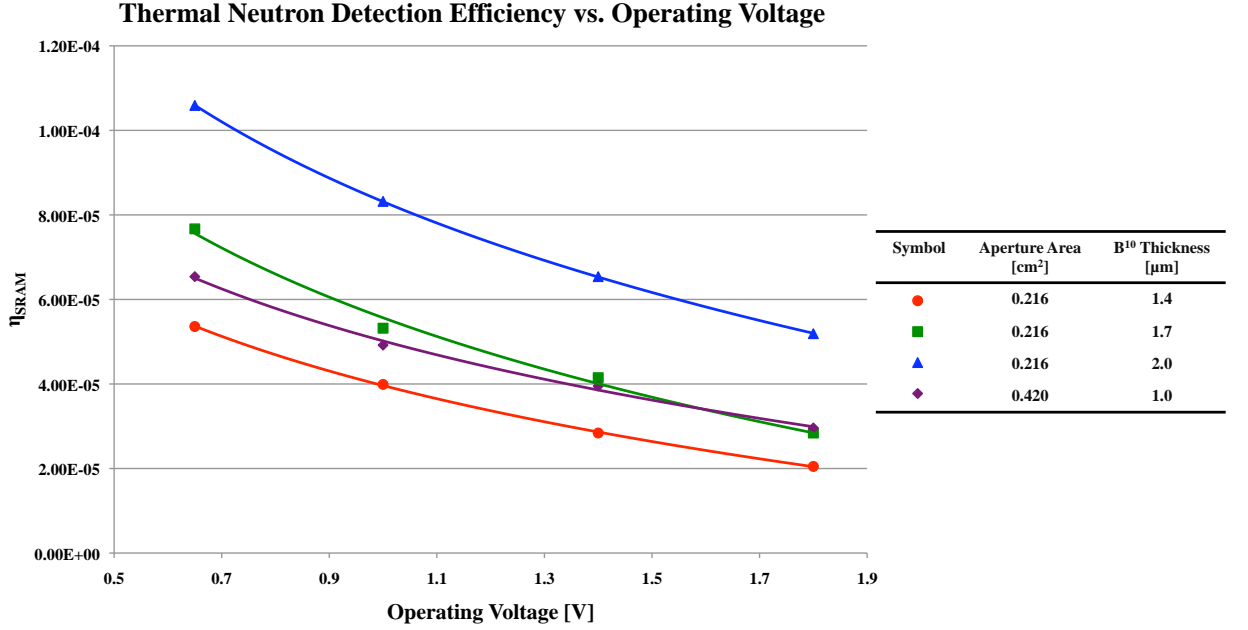


Figure 5.6: η_{SRAM} of B¹⁰ Chips #1–#4 at various core operating voltages. Figure illustrates that B¹⁰ Chip #3 was the most efficient at every core operating voltage tested.

Core Voltage [V]	$S \times 10^5 \left[\frac{\text{SEU}}{\frac{n}{\text{cm}^2}} \right]$			
	B ¹⁰ Chip #1	B ¹⁰ Chip #2	B ¹⁰ Chip #3	B ¹⁰ Chip #4
0.65	1.16 ± 0.35	1.66 ± 0.41	2.29 ± 0.75	2.75 ± 0.44
1.00	0.86 ± 0.24	1.15 ± 0.34	1.80 ± 0.55	2.07 ± 0.28
1.40	0.61 ± 0.19	0.90 ± 0.25	1.41 ± 0.48	1.66 ± 0.25
1.80	0.42 ± 0.12	0.61 ± 0.27	1.12 ± 0.33	1.24 ± 0.19

Table 5.6: S of B¹⁰ Chips #1–#4 at various core operating voltages. Values illustrate that B¹⁰ Chip #4 was the most sensitive at every core operating voltage tested.

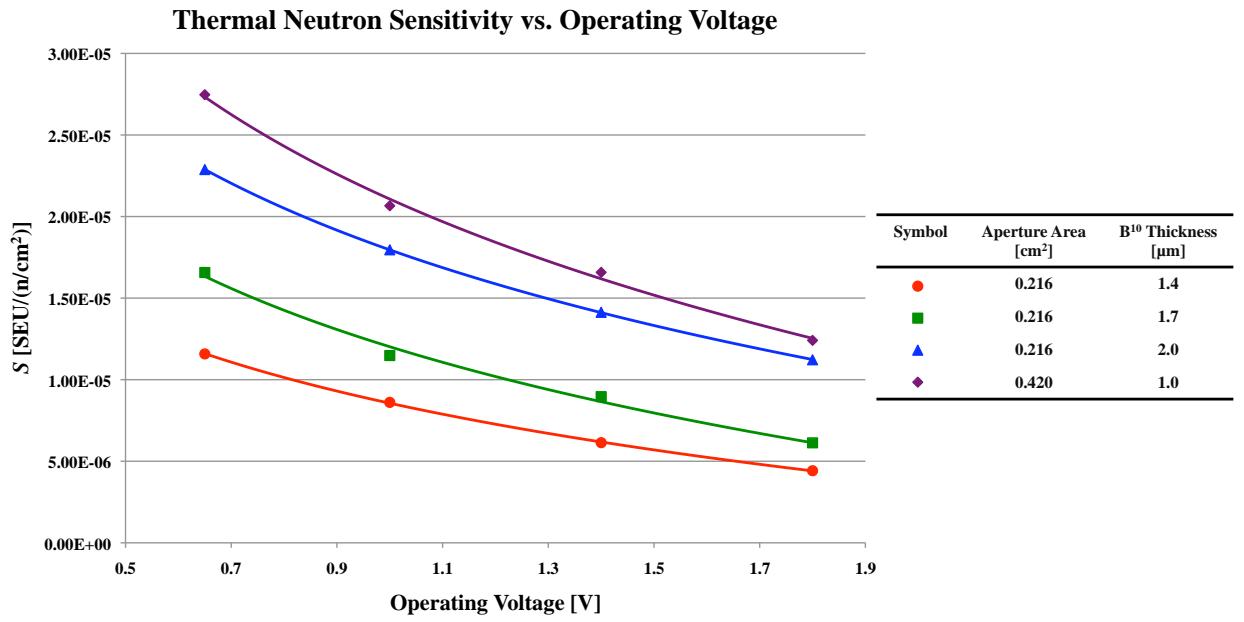


Figure 5.7: S of B¹⁰ Chips #1–#4 at various core operating voltages. Figure illustrates that B¹⁰ Chip #4 was the most sensitive at every core operating voltage tested.

Chapter 6

Detector Comparison, Conclusions and Future Design Recommendations

6.1 Comparison of He³ InterceptorTM and Modified SRAMs

In comparing the He³ InterceptorTM and modified SRAMs, it is important to consider both neutron detection efficiency and power requirements. This project showed that the He³ InterceptorTM was about 200 times more efficient than the most efficient SRAM (B¹⁰ Chip #3 operating at 0.65 V). However, it should be noted that the modified SRAMs' estimated operating time on the same battery the He³ InterceptorTM uses (a sealed, internal, rechargeable, single-cell, 3.7 V, 1.95 Ah lithium-ion battery) is 300 times longer than the InterceptorTM operating in its lowest-power "Surveillance Mode". This mode's estimated operating time was chosen for comparison because it is most comparable to the way SRAMs provide information about the radiation environment. In Surveillance Mode, the Interceptor'sTM LCD screen is off and a slow system clock is used [6]. This data was collected via USB communication with a PC. The information relevant to this comparison is summarized in Table 6.1 on the following page.

	He ³ Interceptor™	Modified SRAM
Current Requirement [mA]	400	0.6
Voltage Requirement [V]	4.4–6	0.65
Estimated Operating Time [h]	60	18,000
η	2.0×10^{-2}	1.06×10^{-4}

Table 6.1: Comparison of He³ Interceptor™ operating in “Surveillance Mode” and B¹⁰ Chip #3 operating at 0.65 V. Surveillance mode is the Interceptor™’s lowest power mode (LCD screen is off and a slow system clock is used). B¹⁰ Chip #3 ($A_{aperture}$ is 0.216 cm², B¹⁰ thickness is 2.0 μ m) operating at 0.65 V is the lowest powered, highest efficiency SRAM. Estimated operating times are for a fully charged 3.7 V, 1.95 Ah lithium-ion battery.

6.2 Modified SRAM Conclusions

As detailed in Chapter 5, this project resulted in several important conclusions that serve as a proof-of-principle for an SRAM-based neutron detection system. Further, it provided insights about several design considerations that will aid chip designers in creating a more efficient and sensitive SRAM-based neutron detection system. This section summarizes those conclusions and makes design recommendations for future generations of the SRAM-based detection system.

This project established that neutron detection efficiency improves at lower core operating voltages, scaling logarithmically. In addition, neutron detection efficiency scaled exponentially with B¹⁰ conversion layer thickness for the chips tested in this project, making B¹⁰ Chip #3 the most efficient at every core operating voltage tested. It should be noted that B¹⁰ thicknesses beyond about 2 μ m will result in decreased neutron detection efficiency due to increased α particle energy loss or stoppage as it traverses the conversion layer. Finally, it showed that while less efficient, an SRAM with a smaller B¹⁰ layer thickness but larger aperture area can result in comparable (and in the case of B¹⁰ Chip #4, greater) neutron detection sensitivity. The results of this project’s characterization of the SRAMs and the resulting conclusions are summarized in Table 6.2 on the next page.

Characterization	Conclusion
Thermal Flux Dependence	η_{SRAM} and S_{SRAM} were not dependent on thermal neutron flux.
Core Operating Voltage Dependence	η_{SRAM} and S_{SRAM} decreased logarithmically with increasing core operating voltage.
B^{10} Conversion Layer Thickness Dependence	η_{SRAM} and S_{SRAM} increased exponentially with increased B^{10} thickness for the B^{10} thicknesses tested (1.0 – 2.0 μm).
η_{SRAM} vs. S_{SRAM}	An SRAM with a smaller B^{10} layer thickness but larger aperture area can result in comparable values for S_{SRAM} .

Table 6.2: Summary of conclusions resulting from experimental characterizations.

6.3 Future Design Recommendations

The SRAMs evaluated in this project were COTS devices that were modified to increase their sensitivity to neutrons. Because they were not designed to detect neutrons, the SRAMs’ efficiencies and sensitivities were limited. Now that the potential for an SRAM-based neutron detection has been established, SRAMs designed specifically for neutron detection can be made much more sensitive. As a result of the information presented in this report, there are several recommendations for future designs. Chips should be able to operate at the lowest core operating voltage achievable and thinner B^{10} layers should be deposited over larger apertures in order to avoid compressive stress issues induced by the B^{10} film. In general, there are also improvements that can be made if chips are being designed specifically for the purpose of radiation detection. First, in a typical SRAM only two of the six SRAM transistors are particularly sensitive to SEUs. In general, the n-type transistors are three times more sensitive than the p-type transistors because of the higher mobility of minority carriers in n-type devices. Future designs should have larger gate areas for the n-type transistors. In addition, the n-type cells should be surrounded with B^{10} . The chips evaluated in this project only had B^{10} below the circuitry. Future models should also have trenches of B^{10} on

Design Consideration	Recommendation
Operating Voltage	Lowest achievable.
B ¹⁰ Thickness and Aperture Area	Efficiency sacrificed due to thinner B ¹⁰ layers needed to prevent damage resulting from compressive stress issues can be compensated for with larger aperture areas.
n-type Gate Area	Should be increased in order to increase sensitive area.
B ¹⁰ Deposition	Deposit B ¹⁰ below, on the sides of, and on top of sensitive nodes.
SRAM Arrays	Stack multiple SRAMs in an array to improve cumulative efficiency and sensitivity.

Table 6.3: Summary of conclusions resulting from experimental characterizations.

the sides of the n-type transistors and on top of the devices in the form of gate contacts made out of B¹⁰. In addition, stacking multiple SRAMs in an array will improve the overall neutron detection efficiency and neutron sensitivity of the SRAM-based detection system. These design recommendations are summarized in Table 6.3.

While the efficiency of the memory-based detection system analyzed in this project was not competitive with the perforated semiconductors being studied at Kansas State University (see Section 2.1), they have much lower power requirements. Additionally, the Kansas State University devices' efficiencies are directly proportional to the applied voltage. The SRAMs evaluated by this project, however, are *more* efficient at lower power. This will be particularly important when used for remote detection of SNM. In addition, future generations of the SRAM detectors have the potential to be significantly more efficient than the ones evaluated in this project, making them competitive with the devices developed by Kansas State University.

Appendix A

Conventional Non-Powered Detection System Results

A.1 Conventional Non-Powered Detection System Limitations and Detection Mechanisms

As mentioned in Section 4.1 on page 36, the non-powered neutron detection systems were not appropriate comparisons for the SRAM-based detection system evaluated in the project. This was due primarily to the fact that the non-powered detection systems are designed for dosimetry. For this reason, the non-powered systems were not used as direct points of comparison for the SRAM-based detection system. Instead the information gleaned from the non-powered detectors provided additional information about the neutron environment.

A.2 Conventional Non-Powered Neutron Detection Systems Results and Suggested Performance Metrics for Future Works

The results obtained from the non-powered detection systems available in the project are summarized in Table A.1 on the following page. As was the case with the majority of the data presented in this report, the uncertainties

Detector	Energy Range	Dose Rate [$\frac{\text{mrem}}{\text{hr}}$]	
		PuBe Slugs	Neutron Generator
TLD (w/o Phantom)	Thermal–14 MeV	34.9 ± 1.7	$21,000 \pm 1,000$
TLD (w/ Phantom)	Thermal–14 MeV	Not Tested	$54,000 \pm 1,000$
Bubble Dosimeter	Thermal	1.8 ± 0.1	Not Tested
Track-Etch Dosimeter	Thermal–40 MeV	19.4 ± 0.6	$17,600 \pm 700$

Table A.1: Thermal neutron sensitivities of B¹⁰ Chips #1 and #2 at various core operating voltages.

provided are purely statistical and represent the standard deviation of the mean. Due to the complicated neutron environment created by the moderation of the source and scattering of the walls and equipment in the generator room, the energy range the detection systems are sensitive to plays an important role in analyzing their results. In addition, the algorithm used to calculate the neutron dose equivalent of the TLDs takes into account radiation interactions with the human body. For this reason, a "phantom" is typically used to simulate a human body during exposures when the TLD is not being worn. The phantom used in this project was a plexiglass box filled with water. It should also be noted that the bubble dosimeters were not exposed to the D-T neutron generator because they would have quickly saturated, potentially resulting in the dosimeter leaking or bursting.

A.3 Conventional Non-Powered Detection System Suggested Performance Metrics for Future Work

While this project did not directly compare the non-powered detection systems to the SRAM-based detection system, it is possible to calculate neutron detection efficiencies for the bubble dosimeters and the track-etch dosimeters. In the case of the TLD, the only information available was neutron dose equivalent.

Bubble dosimeters are read by simply counting the bubbles that appear in the tube after exposure. Since each bubble results from a single neutron interaction, the number of bubbles represented the number of neutrons

the dosimeter detected. Two classes of bubble dosimeters were available for testing, one that is sensitive to thermal neutrons and one that responds to neutrons with energies in the range [200 keV – 15 MeV] (fast neutrons). Thus, the thermal bubble dosimeters were used since their efficiencies could be more directly compared to the modified SRAMs.

While designed to provide the same information as the TLDs, track-etch dosimeters are read by counting the track density on the dosimeter and correlating this value to a radiation dose. The raw neutron track density data, if obtainable, could be used to calculate a pure neutron efficiency. The track-etch dosimeters tested were sensitive to fast, intermediate, and thermal neutrons with the ability to group them into two categories: fast- and intermediate-speed neutrons and thermal neutrons. This dosimeter is composed of a track registering material covered by two radiators. Each radiator covers about half of the chip surface. One radiator is composed of polyethylene and the second radiator is composed of boron-loaded Teflon. The area behind the polyethylene radiator is intended to measure the fast neutron dose. The area behind the boron-loaded Teflon radiator responds to fast and thermal neutrons. The fast neutron dose is proportional with the number of tracks found on the fast side. Thermal neutron dose was calculated by subtracting the polyethylene response from the Teflon radiator response.

A.3.1 Bubble Dosimeter

$$\eta_{\text{Bubble}} = \frac{N_{\text{bubble}}}{(\phi_{\text{thermal}})(A_{\text{tube}})(t_e)} \quad (\text{A.1})$$

Where:

$$\begin{aligned} N_{\text{bubble}} &= \text{number of bubbles in emulsion} \\ \phi_{\text{thermal}} &= \text{thermal neutron flux} \left[\frac{\text{n}}{\text{cm}^2 \cdot \text{s}} \right] \\ A_{\text{tube}} &= \text{cross-sectional area of tube} [\text{cm}^2] \\ t_e &= \text{length of exposure} [\text{s}] \end{aligned}$$

A.3.2 Track-Etch Dosimeter

$$\eta_{\text{Track-Etch}} = \frac{\rho_{\text{track}}}{(\phi_{\text{thermal}})(t_e)} \quad (\text{A.2})$$

Where:

$$\begin{aligned}\rho_{\text{track}} &= \text{thermal neutron track density} \left[\frac{\text{tracks}}{\text{cm}^2} \right] \\ \phi_{\text{thermal}} &= \text{thermal neutron flux} \left[\frac{\text{n}}{\text{cm}^2 \cdot \text{s}} \right] \\ t_e &= \text{length of exposure [s]}\end{aligned}$$

A.4 Recommendations for Future Work

A potential extension of this project could be to conduct a more extensive evaluation of the bubble and track-etch dosimeters, ultimately calculating their neutron detection efficiencies and comparing them to one another as well as the SRAM-based detection system. η for the bubble dosimeter and track-etch dosimeter are defined in Sub-Sections A.3.1 on the previous page and A.3.2 on the preceding page.

Appendix B

Foil Activation Theory and Sample Calculations

The theory outlined in this appendix is supported by References [2] and [21]. Constants throughout were obtained from [22].

B.1 Foil Activation Theory

Neutron measurements can be determined indirectly through radioactivity that is induced in some materials by neutron interactions. In general, the saturated activity induced in a foil, A_∞ [s^{-1}], is:

$$A_\infty = \phi \Sigma_a V \tag{B.1}$$

Where:

$$\begin{aligned} \phi &= \text{average neutron flux over foil surface} \left[\frac{\text{n}}{\text{cm}^2 \cdot \text{s}} \right] \\ \Sigma_a &= \text{average macroscopic absorption cross-section over neutron spectrum} [\text{cm}^{-1}] \\ V &= \text{foil volume} [\text{cm}^3] \end{aligned}$$

Thin metal foils can be exposed to a flux of neutrons for a period of time and then removed so that the induced radioactivity can be read by a detector. In this way, the neutron flux of the source can be calculated.

B.1.1 Thermal Flux Determination

Because it was desirable to determine the thermal flux, indium (In) and cadmium (Cd)-covered indium foils were exposed to the neutron environment and the induced radioactivity was read with a hyper-pure germanium (HpGe) detector. With a high absorbing absorption cross-section for low energy neutrons and a moderately low cross-section for high-energy neutrons, cadmium acts as a neutron filter (i.e. high-energy neutrons penetrate the cadmium shield while low energy neutrons are blocked). In practice, the neutron flux below the cadmium cut-off (0.6 eV) is taken to be the “thermal flux” [2]. The reaction of interest is:



The cadmium ratio, R_{Cd} , is the saturated activity of a bare foil, A_{∞}^b , divided by the saturated activity of a foil completely covered with Cd, A_{∞}^c :

$$R_{Cd} = \frac{A_{\infty}^b}{A_{\infty}^c} \quad (\text{B.2})$$

R_{Cd} can be taken as a measure of the source’s thermalization. The greater the cadmium ratio, the greater the degree of thermalization. The cadmium difference, D_{Cd} , is the saturated activity of a bare foil minus that of the cadmium-covered foil. It equates to the activity produced by neutrons whose energies are less than the cut-off of Cd.

$$D_{Cd} = A_{\infty}^b - A_{\infty}^c = A_{\infty}^{sub-Cd} \quad (\text{B.3})$$

Substituting Equation B.2 into Equation B.3 yields:

$$A_{\infty}^{sub-Cd} = A_{\infty}^b - \frac{A_{\infty}^b}{R_{Cd}} \quad (\text{B.4})$$

Equating Equation B.1 on the previous page and Equation B.4 and accounting for the use of the detector (see [21]):

$$A_{\infty}^b - \frac{A_{\infty}^b}{R_{Cd}} = \epsilon q \Omega \phi_{sub-Cd} \Sigma_a V, \quad (\text{B.5})$$

where:

ϵ = detection efficiency at E_γ

q = γ /disintegration

Ω = fractional solid angle (i.e. probability that γ emitted will enter detector)

Factoring out A_∞^b in Equation B.5 on the previous page yields:

$$\epsilon q \Omega \phi_{sub-Cd} \Sigma_a V = A_\infty^b \left(1 - \frac{1}{R_{Cd}} \right) \quad (B.6)$$

Solving for the sub-cadmium flux, ϕ_{sub-Cd} :

$$\phi_{sub-Cd} = \frac{A_\infty^b (1 - \frac{1}{R_{Cd}})}{\epsilon q \Omega \Sigma_a V} \quad (B.7)$$

A_∞^b is determined by observed foil counts, therefore:

$$A_\infty^b = \frac{\lambda(C - B)}{(1 - e^{-\lambda t_e})(e^{-\lambda t_w})(1 - e^{-\lambda t_c})} \quad (B.8)$$

where:

$$\lambda = \frac{\ln 2}{t_{1/2}}$$

$t_{1/2}$ = half life of In

C = bare foil counts

B = background counts

t_e = exposure time

t_w = wait time

t_c = count time

Substituting Equation B.8 into Equation B.7 yields:

$$\phi_{sub-Cd} = \frac{\lambda_{In}(C - B)(1 - \frac{1}{R_{Cd}})}{\epsilon q \Omega \Sigma_a V f_e f_w f_c}, \quad (B.9)$$

where:

$$f_e = 1 - e^{-\lambda t_e}$$

$$f_w = e^{-\lambda t_w}$$

$$f_c = 1 - e^{-\lambda t_c}$$

Determination of ϵ and Ω will be discussed further in Section B.2.1 on the following page. Note that if the bare and cadmium covered foils have equal exposure times and count times:

$$R_{Cd} = \frac{\left(\frac{C_b}{e^{-\lambda t_{wb}}}\right)}{\left(\frac{C_c}{e^{-\lambda t_{wc}}}\right)}, \quad (\text{B.10})$$

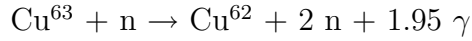
where:

$$\begin{aligned} t_{wb} &= \text{wait time of bare foil} \\ t_{wc} &= \text{wait time of covered foil} \end{aligned}$$

The term “wait time” refers to the amount of time between the removal of the source from the radiation environment and when the detector begins counting the induced radioactivity.

B.1.2 Fast Neutron Flux

Another useful flux measurement is obtained through the use of copper (Cu) foils. Neutrons induce gamma radiation in copper foils through the reaction:



This reaction has a 10 MeV threshold (i.e. the flux calculated will ultimately represent the flux of neutrons with an energy greater than 10 MeV). This will be termed the “fast flux.”

In the case of copper foil activation, a sodium-iodide (NaI) detector was used to detect the 0.51 MeV γ emitted from the (n,2n) interaction with Cu^{63} . It is important, therefore, to determine the NaI detection efficiency (ϵ) for $E_\gamma = 0.51$ MeV. This calculation is detailed in Sub-Section B.2.2 on page 67.

Once the detection efficiency is known, the neutron flux can be determined by:

$$\phi_{fast} = \frac{\lambda_{\text{Cu-62}}(C - B)}{\epsilon q \Omega \Sigma_{a63} V f_e f_w f_c}, \quad (\text{B.11})$$

where:

$$\begin{aligned} \Sigma_{a63} &= \text{macroscopic absorption cross section} \\ &\text{of Cu}^{63} \text{ to 14.3 MeV neutrons [cm}^{-1}\text{]} \end{aligned}$$

This relationships allow for the calculation of the fast flux.

B.2 Sample Calculations

B.2.1 Thermal Flux

In order to calculate the sub-cadmium flux, Equation B.9 on page 62 is employed. A sample calculation is provided below:

$$\phi_{sub-Cd} = \frac{\lambda_{In}(C_b - B_b)(1 - \frac{1}{R_{Cd}})}{\epsilon q \Omega \Sigma_a V f_e f_w f_c}$$

Calculating the decay constant, λ_{In} :

$$\lambda_{In} = \frac{\ln 2}{t_{1/2}} = \frac{\ln 2}{54.2 \text{ min}} = 0.0128 \text{ min}^{-1} = 2.132 \times 10^{-4} \text{ s}^{-1}$$

Bare foil counts, background counts, were obtained experimentally:

$$\begin{aligned} C_b &= 1402 \text{ counts} \\ B_b &= 0 \text{ counts} \end{aligned}$$

R_{Cd} is calculated in accordance with Equation B.10 on the previous page:

$$R_{Cd} = \frac{\left(\frac{C_b}{e^{-\lambda t_{wb}}}\right)}{\left(\frac{C_c}{e^{-\lambda t_{wc}}}\right)} = \frac{\left(\frac{1402 \text{ counts}}{e^{(-2.132 \times 10^{-4} \text{ s}^{-1})(60 \text{ s})}}\right)}{\left(\frac{139 \text{ counts}}{e^{(-2.132 \times 10^{-4} \text{ s}^{-1})(60 \text{ s})}}\right)} = 10.09$$

ϵ is determined for the energy at which gamma rays are emitted by indium through linear interpolation between two known calibration sources licensed to the United States Naval Academy, namely Cs^{137} and Ba^{133} as follows:

$$\epsilon = \frac{\text{net counts}}{I \Omega q t_c 3.7 \times 10^4} \quad (\text{B.12})$$

where:

$$\begin{aligned} I &= I_o e^{-\lambda t} \text{ (present source intensity } [\mu\text{Ci}]) \\ \Omega &= \text{fractional solid angle} \\ q &= \frac{\gamma}{\text{disintegration}} \text{ (decimal fraction)} \\ t_c &= \text{count time} \\ 3.7 \times 10^4 &= \text{conversion factor } \left[\frac{\text{disintegrations}}{\text{s} \cdot \mu\text{Ci}} \right] \end{aligned}$$

Ω represents the fractional solid angle, or the probability that a γ emitted by the foil will enter the detector. This is purely a geometrical probability and can be calculated from the radius of the detector and the distance between the detector and the source. Additionally, for the HpGe detector used for the indium foil activations, the foils are placed directly on top of the detector head to be read, resulting in a 50% chance that an emitted γ will enter the detector. Ω would therefore be 0.50. For Cs^{137} , $E_\gamma = 661.7 \text{ keV}$:

$$\begin{aligned} I_o &= 1.0 \text{ }\mu\text{Ci} \\ \lambda &= \frac{\ln(2)}{t_{1/2}} = \frac{\ln(2)}{30 \text{ years}} = 0.0231 \text{ years}^{-1} \\ t &= 4 \text{ years, } 363 \text{ days} = 4.995 \text{ years (at time of calculation)} \end{aligned}$$

Therefore:

$$I = 1.0 \text{ }\mu\text{Ci} e^{-(0.0231 \text{ year}^{-1})(4.995 \text{ year})} = 0.891 \text{ }\mu\text{Ci}$$

And:

$$\begin{aligned} \text{net counts} &= 264,462 \text{ counts} \\ \Omega &= 0.50 \\ q &= 0.851 \frac{\gamma}{\text{disintegration}} \\ t_c &= 300 \text{ s} \end{aligned}$$

Thus,

$$\epsilon_{\text{Cs-137}} = \frac{264,628}{(0.891)(0.50)(0.851)(300)(3.7 \times 10^4)} = 0.0629$$

For Ba^{133} , $E_\gamma = 356 \text{ keV}$:

$$\begin{aligned} I_o &= 1.03 \text{ }\mu\text{Ci} \\ \lambda &= \frac{\ln(2)}{t_{1/2}} = \frac{\ln(2)}{10.74 \text{ years}} = 0.0645 \text{ years}^{-1} \\ t &= 25 \text{ years, } 26 \text{ days} = 25.071 \text{ years (at time of calculation)} \end{aligned}$$

Therefore:

$$I = 1.03 \text{ }\mu\text{Ci} e^{-(0.0645 \text{ year}^{-1})(25.071 \text{ year})} = 0.204 \text{ }\mu\text{Ci}$$

and:

$$\begin{aligned}\text{net counts} &= 62,054 \text{ counts} \\ \Omega &= 0.50 \\ q &= 0.690 \frac{\gamma}{\text{disintegration}} \\ t_c &= 300 \text{ s}\end{aligned}$$

Thus,

$$\epsilon_{\text{Ba-133}} = \frac{62,054}{(0.204)(0.50)(0.690)(300)(3.7 \times 10^4)} = 0.0794$$

Therefore the detection efficiency for In ($E_\gamma = 417 \text{ keV}$) is determined through linear interpolation to be:

$$\epsilon_{\text{In}} = 0.0761$$

It is known that for In:

$$q_{\text{In}} = 0.277 \frac{\gamma}{\text{disintegration}}$$

Based on the placement between the foil and detector:

$$\Omega = 0.50$$

The macroscopic absorption cross section for indium is determined as follows:

$$\Sigma_a = N\sigma_a,$$

where:

$$\begin{aligned}N^{\text{In-166}} &= (\text{isotopic abundance of In}^{166})(N^{\text{In}}) \\ &= (0.957) \left(0.0348 \frac{\text{atoms}}{\text{cm}^3} \right) \\ &= 0.0367 \times 10^{24} \frac{\text{atoms}}{\text{cm}^3} \\ \sigma_a &= 81 \times 10^{-24} \text{ cm}^2 \\ &= 81 \text{ b}\end{aligned}$$

Therefore:

$$\begin{aligned}\Sigma_a &= \left(0.0367 \times 10^{24} \frac{\text{atoms}}{\text{cm}^3} \right) (81 \text{ b}) \\ &= 2.97 \text{ cm}^{-1}\end{aligned}$$

Volume is calculated using the mass of the foil and the density of indium:

$$V = \frac{m_{\text{foil}}}{\rho} = \frac{0.50 \text{ g}}{7.31 \frac{\text{g}}{\text{cm}^3}} = 0.0684 \text{ cm}^3$$

The time constants are calculated based on the exposure, wait, and count times used in the foil activation experiment as follows:

$$\begin{aligned} f_e &= 1 - e^{-\lambda_{\text{In}} t_e} = 1 \text{ (saturated)} \\ f_w &= e^{-\lambda_{\text{In}} t_w} = e^{-(2.131 \times 10^{-4} \text{ s}^{-1})(60 \text{ s})} = 0.987 \\ f_c &= 1 - e^{-\lambda_{\text{In}} t_c} = 1 - e^{-(2.131 \times 10^{-4} \text{ s}^{-1})(3600 \text{ s})} = 0.536 \end{aligned}$$

Finally, we calculate the sub-cadmium (or thermal) flux:

$$\begin{aligned} \phi_{\text{sub-Cd}} &= \frac{(2.131 \times 10^{-4} \text{ s}^{-1})(1402 \text{ counts}) \left(1 - \frac{1}{10.06}\right)}{(0.0761) \left(0.277 \frac{\gamma}{\text{dis}}\right) (2.97 \text{ cm}^{-1})(0.0684 \text{ cm}^3)(1)(0.987)(0.536)} \\ &= 240 \frac{\text{n}}{\text{cm}^2 \cdot \text{s}} \end{aligned}$$

B.2.2 Fast Flux

In order to calculate the fast flux using Cu foils, it is first important to determine the NaI detection efficiency at the appropriate E_γ . This is calculated in accordance with Equation B.12 on page 64 using a Na^{22} source which produces $E_\gamma = 0.51 \text{ MeV}$. For the Na^{22} source used:

$$\begin{aligned} I_o &= 0.9117 \text{ } \mu\text{Ci} \\ \lambda_{\text{Na}-22} &= \frac{\ln(2)}{t_{1/2}} = \frac{\ln(2)}{2.6 \text{ years}} = 0.267 \text{ years}^{-1} \\ t &= 5 \text{ years, 1 day} = 5.003 \text{ years (at time of calculation)} \end{aligned}$$

Therefore, the source intensity at the time of calculation is:

$$I = 0.9117 \text{ } \mu\text{Ci} e^{-(0.267 \text{ year}^{-1})(5.003 \text{ year})} = 0.240 \text{ } \mu\text{Ci}$$

Unlike the germanium detector used to determine the thermal flux, the foil does not lay directly on the detector face so the fractional solid angle cannot be taken as 0.50. Based on the geometry of the detector, it was determined that:

$$\Omega = 0.262$$

Additionally:

$$\begin{aligned} q_{\text{Na-22}} &= 1.81 \frac{\gamma}{\text{disintegration}} \\ t_c &= 100 \text{ s} \end{aligned}$$

Therefore:

$$\epsilon_{\text{Na-22}} = \frac{91\,819}{(0.240)(0.262)(1.81)(100)(3.7 \times 10^4)} = 0.218$$

Because both Na²² and Cu emit 0.51 MeV γ :

$$\epsilon_{\text{Na-22}} = \epsilon = 0.218$$

With the detector efficiency determined, Equation B.11 on page 63 can be used to calculate the fast flux. A sample calculation is included below:

$$\phi_{fast} = \frac{\lambda_{\text{Cu-62}}(C - B)}{\epsilon q \Omega \Sigma_{a63} V f_e f_w f_c}$$

Where:

$$\begin{aligned} \lambda_{\text{Cu-62}} &= \frac{\ln 2}{t_{1/2}} = \frac{\ln 2}{594 \text{ s}} = 1.17 \times 10^{-3} \text{ s}^{-1} \\ C &= 1,584 \text{ counts} \\ B &= 0 \text{ counts} \\ q_{\text{Cu-62}} &= 1.95 \frac{\gamma}{\text{disintegration}} \\ f_w &= e^{-\lambda_{\text{Cu-62}} t_w} = e^{-(1.17 \times 10^{-3} \text{ s}^{-1})(120 \text{ s})} = 0.869 \\ f_c &= 1 - e^{-\lambda_{\text{Cu-62}} t_c} = 1 - e^{-(1.17 \times 10^{-3} \text{ s}^{-1})(100 \text{ s})} = 0.110 \\ f_e &= 1 - e^{-\lambda_{\text{Cu-62}} t_c} = 1 - e^{-(1.17 \times 10^{-3} \text{ s}^{-1})(300 \text{ s})} = 0.296 \end{aligned}$$

To determine Σ_{a63} , the following relationship is used:

$$\Sigma_{a63} = N_{63} \sigma_{a63}$$

Where:

$$\begin{aligned} N_{63} &= \text{Cu}^{63} \text{ atom density (69.1\% of natural Cu)} \\ &= (0.691)(0.08493 \times 10^{24}) = 0.0587 \times 10^{24} \frac{\text{atoms}}{\text{cm}^3} \\ \sigma_{a63} &= \text{Cu}^{63} \text{ microscopic absorption cross section for 14.3 MeV neutrons} \\ &= 0.53 \text{ b} \end{aligned}$$

Therefore:

$$\Sigma_{a63} = \left(0.0587 \times 10^{24} \frac{\text{atoms}}{\text{cm}^3} \right) (0.53 \text{ b}) = 3.11 \times 10^{-2} \text{ cm}^{-1}$$

Volume is calculated using the mass of the foil and the density of Cu:

$$V = \frac{m_{\text{foil}}}{\rho} = \frac{3.84 \text{ g}}{8.96 \frac{\text{g}}{\text{cm}^3}} = 0.429 \text{ cm}^3$$

Finally, the fast flux can be calculated:

$$\begin{aligned} \phi_{fast} &= \frac{(1.17 \times 10^{-3} \text{ s}^{-1})(1,584 \text{ counts})}{(0.218) \left(1.95 \frac{\gamma}{\text{dis}}\right) (0.262)(3.11 \times 10^{-2} \text{ cm}^{-1})(0.429 \text{ cm}^3)(0.869)(0.110)(0.296)} \\ &= 9.5 \times 10^4 \frac{\text{n}}{\text{cm}^2 \cdot \text{s}} \end{aligned}$$

Bibliography

- [1] H. Cember, *Introduction to Health Physics*. New York: Pergamon Press, Inc., 1983.
- [2] G. F. Knoll, ed., *Radiation Detection and Measurement*. New York: John Wiley & Sons Inc., 2000.
- [3] H. Ing, R. A. Noulty, and T. D. McLean, “Bubble detectors—a maturing technology,” *Radiation Measurements*, vol. 27, no. 1, pp. 1–11, 1996.
- [4] Bubble Technology Industries, “Neutron dosimeters technical specifications,” 2009. www.bubbletec.ca.
- [5] Landauer, “Neutrak dosimeter for neutron radiation technical specifications,” 2006. www.landauerinc.com.
- [6] Thermo Fisher Scientific, Inc., *Interceptor Spectroscopic Personal Radiation Detectors User’s Manual*, 2007.
- [7] D. S. McGregor, S. L. Bellinger, D. Bruno, S. A. Cowley, W. L. Dunn, M. Elazequi, S. Karger, M. McNeil, H. Oyenian, E. Patterson, J. K. Shultis, G. Singh, C. J. Solomon, and T. C. Unruh, “Wireless neutron and gamma ray detector modules for dosimetry and remote monitoring,” in *IEEE Nuclear Science Symposium Conference Record, 2007. NSS ’07. IEEE*, vol. 1, pp. 808–812, Nov. 2007.
- [8] D. S. McGregor, S. L. Bellinger, D. Bruno, S. A. Cowley, M. Elazequi, M. McNeil, E. Patterson, T. C. Unruh, C. J. Solomon, J. K. Shultis, and B. B. Rice, “Perforated semiconductor neutron detector modules for detection of spontaneous fission neutrons,” in *Technologies for Homeland Security, 2007 IEEE Conference on*, pp. 162–167, May 2007.

- [9] J. F. Ziegler, 2010. Private communication.
- [10] R. Baumann, “Soft errors in commercial integrated circuits,” *International Journal of High Speed Electronics and Systems*, vol. 14, no. 2, pp. 299–309, 2004.
- [11] J. F. Ziegler, ed., *SER–History, Trends and Challenges: A Guide for Designing with Memory ICs*. San Jose: Cypress Semiconductor Corporation, 2004.
- [12] G. E. Moore, “Cramming more components onto integrated circuits,” *Electronics*, vol. 38, no. 8, pp. 201–225, 1965.
- [13] Honeywell International Inc., “HXS6408 512k x 8 STATIC RAM Technical Specifications,” 2009. www.honeywell.com.
- [14] J. D. Plummer, M. D. Deal, and P. B. Griffin, *Silicon VLSI Technology: Fundamentals Practice and Modeling*. New Jersey: Prentice Hall, 2000.
- [15] H. O. Pierson, *Handbook of Chemical Vapor Deposition: Principles, Technology and Applications*. New Jersey: Noyes Publication, 1992.
- [16] S. Koev, “Instrumentation to test the avionics of the new joint strike fighter,” 2004. United States Naval Academy Capstone Final Report.
- [17] D. S. McGregor, M. D. Hammig, Y. H. Yang, H. K. Gersch, and R. T. Klann, “Design considerations for thin film coated semiconductor thermal neutron detectors—I: Basics regarding alpha particle emitting neutron reactive films,” *Nuclear Instruments and Methods in Physics Research*, vol. 500, pp. 272–308, 2003.
- [18] J. F. Ziegler, “SRIM (the stopping and range of ions in matter) software,” 2010. Software available for download from www.SRIM.org.
- [19] D. E. Fulkerson and E. E. Vogt, “Prediction of soi single-event effects using a simple physics-based spice model,” *IEEE Transactions on Nuclear Science*, vol. 52, no. 6, 2005.
- [20] M. Liu, 2010. Private communication.
- [21] J. B. Hoag, ed., *Nuclear Reactor Experiments*. New Jersey: D. Van Nostrand Company, Inc., 1958.

- [22] J. R. Lamarsh and A. J. Baratta, eds., *Introduction to Nuclear Engineering, Third Edition*. New Jersey: Prentice Hall, 2001.
- [23] J. I. Katz, “Detection of neutron sources in cargo containers,” *Science and Global Security*, vol. 14, pp. 145–149, 2006.
- [24] P. J. McMarr, M. E. Nelson, S. T. Lui, D. Nelson, K. J. Delikat, P. Gouker, B. Tyrell, and H. Hughes, “Asymmetric SEU in SOI SRAM,” *IEEE Transactions on Nuclear Science*, vol. 52, no. 6, pp. 2481–2486, 2005.